University of Zurich[UZH]

Illumination Artifacts in Radiance-Based SIF Retrievals Using Oxygen Bands: A Study Over Complex Forest Structures

ESS 511 Master's Thesis

Author
Patrik Muggli
12-472-965

Supervised by
Prof. Dr. Alexander Damm

Faculty representative
Prof. Dr. Alexander Damm

01.10.2023
Department of Geography, University of Zurich

Illumination Artifacts in Radiance-Based SIF Retrievals Using Oxygen Bands: A Study Over Complex Forest Structures

Patrik Muggli

October 1, 2023

Abstract

Solar-induced chlorophyll fluorescence (SIF) is a unique optical signal, offering a remote sensing (RS) window into photosynthetic energy conversion and carbon uptake and provide the opportunity to track these mechanisms over a wide range of spatial scales.
Unfortunately, SIF emission is only a subtle signal that overlaps with radiation reflected by the Earth's surface, making radianc-based SIF retrievals susceptible to errors.
While recent advancements in optical RS sensors enable the measurement of upwelling radiance ($L_{\uparrow}$) on a high spectral and spatial resolution, the accurate estimate of the surface irradiance field (E) is still very limited. Downwelling light fluxes ($E_{\downarrow}$) are often estimated globally by assuming that the surface beneath is uniformly illuminated. This practice not only leads to a spatial mismatch between the measured E and L fluxes but also induce errors when surfaces become heterogeneous.
The assumption of a fully illuminated surface does not hold, when applied to intricate vegetation, like vertically structured forests where the interplay between sunlit and shaded patterns results in varying proportions of diffuse and direct irradiance (E_{dir}, E_{dif}) along the vegetation surface. Given the fact that both E components exhibits different absorption band depths in the O_2A feature, the lack of knowledge about the incident light field can lead to infilling artifacts in SIF retrievals using oxygen bands.

To quantify the magnitude and dynamics of illumination uncertainties in heterogeneous vegetation bodies, a modeling experiment was established, where top of canopy SIF was simulated over a realisitc 3D virtual forest scene and contrasted with retrievals from three fundamental algorithms (sFLD, 3FLD, iFLD). To properly decouple the illumination error (ε_{ill}) from the overall retrieval bias (ε_{tot}), a new modeling approach was developed. The coupled atmosphere-vegetation radiative transfer was simulated under use of DART model.

Illumination artifacts were found to be highly dynamic in space, time, and showed significant sensitivity on the footprint of the observation.
At finer leaf scale, relative illumination errors exhibited substantial fluctuations, ranging from almost negligible ($\approx$ 0%) to a substantial 180% (ARE_{mean}=23%, ARE_{Q95}=81%). By up-scaling the observations to the ecosystem level, the variability converged and stabilized consistently, falling within a narrow 4-9% range.
Despite the scale dependency, illumination uncertainties manifested notable spatio-temporal fluctuations controlled by the atmosphere RT. They peaked at midday, coinciding with the maximal spectral differences between sun and sky light, and diminished during morning and evening.
Further the canopy RT was identified to be highly involved in the formation of illumination artifacts. Particularly strong multiple scattering in the NIR spectrum, played a pivotal role in shaping the magnitude of these errors.

Contents

List of Figures

1 Introduction

Passive remote sensing (RS) of solar-induced chlorophyll fluorescence (SIF or F) is a growing topic in the scientific community because of its potential to monitor photosynthesis and plant stress on a global level [3]. In the past decades radiative-based SIF retrievals using oxygen bands were extensively used in a wide range of ecosystem studies on various spatial and temporal scales [46].

The retrieved top-of-canopy (TOC) fluorescence signal, however, is complex in nature and difficult to interpret since variations cannot be directly related to the physiological status of the vegetation. Instead, they are also influenced by several confounding effects arising from the canopy structure, vegetation biochemistry, observation scale and illumination-observer geometries [72]. Moreover, fluorescence emission is only a minuscule signal that overlaps with the surface reflected radiance (L_R), making retrieval methods and setups susceptible to various errors.

In the past decades, the accuracy of SIF retrievals using O_2 absorption features has been evaluated through various modeling studies and controlled experiments. While these investigations mostly focused on retrieval uncertainties arising from (i) instrumental characteristics [10, 22, 33], (ii) methodological restrictions of applied algorithms [45, 2, 7], and (iii) effects arising from atmosphere radiative transfer (RT) [22, 62, 57, 56, 35], there is a notable scarcity in systematic evaluations incorporating the quantitative impact of canopy structure on potential retrieval artifacts.

In this context it is important to mention that the early retrieval methods were developed with a focus on studying the fluorescence emission from individual leaves or canopies with relatively homogeneous vegetation, such as agricultural fields or controlled laboratory experiments. Applying these algorithms over complex and heterogeneous vegetation like forests leads to considerable complications since accurate measurement of incoming and outgoing fluxes become challenging.

Indeed, there is a fundamental issue of current measurement setups using a top of canopy (ToC) approach which has not been adequately discussed in the literature so far. Incoming light is only estimated globally by measuring the incident downwelling irradiance from a reference board above the canopy ($E_{\downarrow ToC}$) while assuming the vegetation surface beneath as fully illuminated. Canopies, however, are inherently structured 3D objects, containing leaves and branches. The presence of overlapping foliage and canopy gaps can cause varying degrees of shelf- or cast- shadows where direct light is fully or partly blocked, creating complex and spatially heterogeneous surface irradiance fields [47, 11, 30]. The globally estimated $E_{\downarrow ToC}$, currently used as input to SIF retrieval algorithms, does not accurately represent the dynamic variation of direct and diffuse irradiance (E_{dir}, E_{dif}) incident on the surface of photosynthetically active canopy elements. Since diffuse light have experienced a higher level of atmospheric absorption during radiative transfer it has formed deeper oxygen absorption band depths (ABD) than direct light [12, 11]. Not correcting for this effect can lead to potential infilling artifacts by radiance-based algorithms, resulting in an underestimation of the truth SIF signal under shaded conditions.

While low-resolution imagery are mixed, consisting of both sunlit and shaded vegetation, the impact of shadows is typically spread over a large area [75, 1]. Enhanced spatial resolution, however, increases the apparent heterogeneity of vegetation surfaces in terms of shadowing or reflectance anisotropy [11] and hence, potentially amplifies local retrieval uncertainties trough inter-pixel variability. The ongoing trend to combine high spectral with high spatial resolution offers new opportunities but also underscore the growing necessity for accurate surface irradiance estimates to overcome uncertainties in such RS observations [14].

Of course, not only fluorescence retrievals are affected by illumination uncertainties. The longer atmospheric path length of E_{dif} as a result of non-isotropic aerosol scattering [58] cause complex wavelength dependent differences in radiation intensity and spectral signature for both E components over the whole RS relevant spectral range (VIS to NIR). For example, the dominant influence of atmospheric Rayleigh scattering $\propto \lambda^{(-4)}$ and Mie scattering towards shorter wavelengths leads to a proportionally higher radiation fraction for diffuse light in the blue spectral region. The lack of knowledge about the incident E field, particularly local variations in E_{dir} and E_{dif}, can lead to wavelength-specific uncertainties in the apparent reflectance (r_{app}) (i.e., pixelwise over- and underestimations) that non-linearly propagate into derived vegetation indices (VIs) and its derived information[11, 75].

To date only few studies have investigated the impact of changing surface E field on RS observations [11, 30, 75, 15, 61], reporting significant relative errors (RE) for both, reflectance-based VIs (RE: ≈5-30%, dependent on VI and study) and radiance-based fluorescnce retrievals (RE up to 58%). Nonetheless, these studies primarily focused on single leafs or simple canopy geometries and do not adequately assess the scale dependency of the problem.

In vertically structured forests, the canopy RT is extremely complex and illumination artifacts are influenced by all types of scattering, including isotropic, volumetric, and geometric-optical. [11, 30]. For 1D radiative

transfer models (RTMs) like mSCOPE [73] it is not possible to assess the anisotropic surface irradiance arising from the canopy 3D structure as a possible source of artefacts in RS of SIF [53]. The integration of fluorescence modules into physically based three-dimensional (3D) RTMs in the earlier past (e.g., DART [19], FluorFLIGHT [24], FluorWPS [76]) make it now possible to reproduce SIF radiative budget from architecturally distinct canopies in full bidirectional reflectance distribution function (BRDF) scenarios. Such forward models are important for bridging scales since they are able to physically downscale RS observations to a leaf level and enable a detailed assessment of the canopy RT [53].

Within the context of the still incomplete SIF uncertainty budget, the main goal of this thesis is to quantify the retrieval uncertainty arising from wrong irradiance input into algorithms over complex 3D vegetation structures.
To achieve this aim, a modelling experiment was established, where SIF was simulated within three distinct scenarios: a realistic virtual 3D forest scene, its vertically homogenized version, and its fully homogenized version. These simulations were then contrasted with SIF retrievals from three fundamental retrieval algorithms: sFLD, 3FLD, and iFLD. The coupled atmosphere-vegetation radiative transfer (RT) of both downwelling and upwelling direct and diffuse fluxes, including SIF radiance, was simulated using DART model. A specialized modeling approach, which simulates fluxes at various heights, was employed to precisely isolate illumination artifacts from other error sources in the SIF retrieval.
Conducting a high-resolution canopy RT analysis over an entire daily cycle facilitated the quantification and comprehension of the spatio-temporal dynamics of illumination artifacts.

2 Theoretical Background

To accurately assess the effects of incomplete knowledge about the irradiation field on the precision of SIF retrieval output, it is crucial to first gain a basic understanding about the physiological response of SIF to changing light conditions (Chapter 2.1) and the potential error sources arising during radiance-based SIF retrievals (Chapter 2.2).

2.1 Physiological Response of SIF on Changing Light Conditions

2.1.1 Origin of Chlorophyll Fluorescence

When a chlorophyll-a pigment is hit by a photon, it converts from the ground state to an excited state depending on the photon-energy [50]. Typically, radiation between 400-700nm, provide enough energy for such a transition. While the majority of excited electrons funneled effectively to photochemical processes for carbon fixation, a small fraction, typically 0.5-3% [32] of the absorbed PAR returns to its ground state by dissipating some of its absorbed energy through internal conversion [50]. This results in the re-emission of photons with reduced energy at longer wavelengths (Stokes shift), giving SIF its additive nature in relation to surface reflected radiance (L_R). The spectral characteristic of the SIF signal is well-defined and exhibits two peaks, in the red region at 685nm and in the far red-region at 740nm [46].

In a general sense, leaf-level fluorescence can be estimated as the product of absorbed photosynthetically active radiation (APAR) and a factor representing the fluorescence efficiency, denoting the ratio of emitted photons to absorbed photons. Therefore, the sum of all SIF photons at a given wavelength (λ) emitted by a single leaf in all directions can be represented as [23]:

$$SIF(\lambda) = PAR \times fPAR_{CHL} \times \Phi_F(\lambda) \tag{1}$$

, where PAR is the photosynthetic active radiation [400-700nm] , $fPAR_{CHL}$ denotes to the fraction of PAR absorbed by chlorophyll, and Φ_F represents the quantum yield of fluorescence. All three quantities are subject to alterations under varying illumination conditions, although the timescales of response for the involved processes may differ.

2.1.2 Sensitivity of APAR on Changing Light Conditions:

From Eq. (1) it is obvious that changing light conditions on the leaf surface, e.g., due to the change from clear sky conditions to cloudy weather or due to light interception (self-, or cast shadows), lead to a decrease of incident PAR, which immediately reduces fluorescence emissions of the leaf (at least under constant fPAR_{CHL} and Φ_F). The ability of a leaf to absorb photons within the 400-700nm range (fPAR_{CHL}), however, is not

constant in time but in a first order determined by the chlorophyll (CHL) pigment-density. In the short term (seconds to minutes), leaves employ various mechanisms to adapt to shaded or sunlit conditions, including state transitions between Photosystem I (PSI) and Photosystem II (PSII), modifications in the number of PSII reaction centers, antenna sizes or absorption cross sections [50]. Over longer periods (days to seasons), leaves in persistent shade (e.g., bottom of canopy) undergo significant physiological and morphological changes, including the investment in light-harvesting structures [20, 43].

2.1.3 Sensitivity of Fluorescence Yield Φ_F on Changing Light Conditions:

To understand the response of Φ_F on changing illumination conditions a fundamental understanding of the energy partitioning at the photosystem level is needed. The main quenching mechanisms of excited chlorophyll experience very fast kinetics (picoseconds to nanoseconds) [50] which is why the fluorescence yield reacts immediately to changing light conditions. Absorbed light energy follow three main dissipating pathways to bring excited electrons quickly to their ground state: (i) photosynthesis (or photochemical quenching, PQ), (ii) non-radiative relaxation, where the excess energy is dissipated as heat (non-photochemical quenching, NPQ), and (iii) radiative relaxation, where the excess energy is emitted in the form of fluorescence [44].
Under low light conditions and without the presence of stressors the main part of APAR is used for PQ under inhibiton of NPQ. Thus, fluorescence emission is one of the processes that dissipate the excess light and the photochemical yield (Φ_P) is inversly related to the fluorescence yield (Φ_F) [16].
On the other hand, when plants are exposed to high levels of excessive light (on a diurnal scale, during peak light hours), the photosynthetic electron transport chain becomes saturated. To avoid oxidative damage trough the building of harmful reactive singlet oxygen species (O_1D) excess excitation energy is increasingly dissipated as thermal energy through non-photochemical quenching (NPQ) pathways [50]. Under these conditions, both (Φ_P) and (Φ_F) decrease proportionally under the action of NPQ (positive relation) [9].
However, it is important to mention that SIF emission has no known physiological or ecological use to plants, is not directly regulated, and has a minuscule impact on the energy budget of plants. Because plants only actively regulate photochemical (PQ) and non-photochemical (NPQ) processes, the dynamics of SIF emission spontaneously reflect, but are not directly controlled by, these regulations [60].

2.1.4 SIF on a Canopy Scale:

Scaling up from the leaf level to the canopy level introduces substantial complexities arising from the interaction and superimposition between plant physiology and physical effects induced by 3D canopy structure, which becomes more complex with higher spatial resolution [63]. The complexities arising from radiative transfer spanning the leaf-to-canopy scale can be primarily viewed from a physical perspective where the fluorescence observed at the top of canopy (SIF_{Obs}) is only a fraction of the total SIF emission by the plants (SIF_{Total}) [74]:

$$SIF_{\text{total}}(\lambda) = \sum_{i=1}^{L} PAR_i(\lambda) \times fPAR_{abs,i}(\lambda) \times \Phi_{f,i}(\lambda) \tag{2}$$

$$SIF_{\text{obs}}(\lambda, \Omega_v) = SIF_{\text{total}}(\lambda) \times f^{\text{esc}}(\lambda, \Omega_v) \tag{3}$$

Eq.(2) describe the total SIF at a certain retrieval wavelength as the cumulative sum of fluorescence contributions from each individual leaf within the canopy, before considering radiative transfer effects. Of course, upon emission from the leaf, the photons which comprise SIF_{Total} are scattered and re-emitted on their way through the foliage and only a fraction, $f^{\text{esc}}(\lambda, \Omega_v)$, ultimately escape the canopy into the viewing direction Ω_v. In complex structured vegetation like forests, canopy anisotropy, influenced by factors such as leaf area index (LAI), leaf orientation (LAD), and woody components, results in a pronounced directionality of the SIF escape factor [53, 34, 42, 27, 52, 39]. Moreover, because of the wavelength dependent leaf optical properties, the re-absorption of the red fluorescence is much more intense than in the far-red, hence, $f^{\text{esc}}(\lambda, \Omega_v)$ exhibits a red edge pattern very similar to vegetation reflectance [60].

2.1.5 Implications for the Modeling Experiment:

From the theory discussed in the previous sections, valuable insights can be deviated for the modeling experiment. Top of canopy SIF results from three primary processes: absorption of incident PAR by chlorophylls (2.1.2), emission of fluorescence by photosystems (2.1.3), and scattering and re-absorption of the emitted fluorescence within the canopy (2.1.4). While the SIF emission is governed by plant physiological mechanisms

(internal energy partitioning), PAR absorption and SIF scattering are primarily controlled by physical factors, including the canopy's 3D structure and the sun-observer geometries [63]. At high spatial resolution, the physical obstruction of PAR in complex vegetation largely dictates SIF emission and variations in the fluorescence signal mainly reflect local PAR changes rather than the plant's physiological status.
As a consequence, the illumination uncertainties caused by the blocking of E_{dir} in shaded features (focus of this thesis), are expected to be superimposed by the physiological change of the true fluorescence emission in response to (physical) PAR blocking in shadows. These two proceses operate independently of each other and affect different wavelength ranges (PAR blocking: VIS, E_{dir} blocking: NIR).
Since APAR is expected to be the main process controlling the SIF variability, it makes sense to model the fluorescence emission with a constant fluorescence yield and consistent biochemical properties, such as CHL content in the context of this thesis. This approach would optimize the consistency in comparing illumination artifacts between pixels, while minimizing potential side effects due to variable plant physiological responses.

2.2 Error Assessment of Radiance-Based SIF Retrievals:

Despite the complications described in the previous section, the well-defined spectral characteristic of the SIF signal, specifically its Stokes shift, enables the measurement of SIF using optical sensors. However, passive RS fluorescence measurements are complicated by the fact that the SIF emission represents only a small fraction of APAR and spectrally overlaps with radiation reflected by Earth surface elements [45] (, which means that emitted SIF and canopy-reflected radiance (L_R) is simultaneously observed by a spectrometer).
Although, the decoupling of SIF from total at sensor radiance (L↑) is challenging, the additive character of SIF (with respect to L_R) can be used to detect the subtle fluorescence signal in regions of the spectra where the incoming irradiance (E↓) is strongly attenuated by the atmosphere of the Sun or Earth. Therefore, radiance-based SIF retrieval algorithms use the "in-filling" of solar Frauenhofer lines or atmospheric O_2 telluric absorption feautures (O_2B [687 nm], O_2A [760 nm]) to increase the relative contribution of SIF to the measured upwelling at sensor radiance ($L = L_R + F$) [2]. Please note that the focus of this study was exclusively on fluorescence retrievals within the O_2A band.

To understand the error sources that can arise during the retrieval process, a basic understanding of the coupled atmosphere-vegetation radiative transfer is needed.
According to the analytical four-stream theory proposed by Verhof and Bach [64], the total downwelling irradiance (E) incident on a flat, homogeneous, fully illuminated, and non-Lambertian vegetation surface basically consists of two fluxes, the direct irradiance from the sun (E_λ^{sun} or E_λ^{dir}), and the diffuse flux from the sky (E_λ^{sky}).

$$E_{\text{surface}} = E_{\text{sun}} + E_{\text{sky}} \tag{4}$$

E_{sun} follows a straight path through the atmosphere without scattering by molecules or aerosols. As a result, it is primarily influenced by the Sun's blackbody radiation spectrum and absorption by atmospheric gases. It can be described as the atmospheric attenuation of extraterrestrial direct irradiance (E^0) by a direct transmittance (τ_{ss}), whereby the radiant energy received by the surface is proportional to the cosine of the solar zenith angle θ_{s} (SZA).

$$E_{\text{sun}} = \tau_{\text{ss}} E^0 \cos\theta_{\text{s}} \tag{5}$$

The diffuse sky radiation, on the other hand, experienced multiple scattering on its way to a specific surface element. It can be approximated as the diffusely transmitted (τ_{sd}) direct solar flux (E^0) under consideration of cosine law, in combination with the back-reflected diffuse upward flux (E^+) from the target, its surroundings, and the atmosphere.The fraction of backscattered upward flux can be described by the spherical albedo of the atmosphere ρ_{dd}.

$$E_{\text{sky}} = \tau_{\text{sd}} E^0 \cos\theta_{\text{s}} + \rho_{\text{dd}} E^+ \tag{6}$$

The radiance signal (L_{TOC}), recorded by a sensor observing the canopy from a certain distance, encompasses the reflected direct and diffuse fluxes, the additive fluorescence emission, and two additional terms to characterize atmospheric modifications to the upwelling flux:

$$L_{\text{TOC}}(\lambda) = \left(\frac{r_{\text{so}} E_\lambda^{\text{sun}} + r_{\text{do}} E_\lambda^{\text{sky}}}{\pi} + f_\lambda^{\text{esc}} F_\lambda^{\text{tot}} \right) \tau_\lambda + L_\lambda^{\text{p}} \tag{7}$$

, where r_{so} is the bi-directional reflectance factor (BRF) of the target and r_{do} is the hemispheric–directional reflectance factor (HDRF) of the target, τ_λ the uwelling atmospherical transmittance between the sensor and the traget, and L_λ^{p} represents the path scattered radiacne.

Given the complexities associated with the intertwined radiative transfer in the vegetation and atmosphere system, as well as challenges posed by the top of canopy (ToC) approach, certain assumptions are often made in real-world applications to distinguish F from L_R. In its basic form, without additional corrections, the FLD method operates under the assumption that:

(A1) Both canopy reflectance (r) and fluorescence emission (F) can be considered as Lambertian, while the hemispherical downwelling irradiance (E) can be treated as isotropic.

(A2) The path between the target and the sensor is short enough to neglect atmospheric transmission (τ_λ) and path radiance (L_λ^p).

(A3) The irradiance flux (E) can be globally measured above the canopy as the vegetation within the sensor's field of view (FOV) is uniformly illuminated. Hence, there is no need to subdivide E into its direct and diffuse fractions.

Given these assumptions, Equation (7) can be reformulated and the radiance signal (L) captured by a sensor observing the canopy simplifies to:

$$L_{\mathrm{TOC}_\lambda} = \frac{r}{\pi} E_{\mathrm{TOC}_\lambda} + F_\lambda^{\mathrm{obs}} \tag{8}$$

From this basis on, far-red F radiance (at λ_{in}=760nm) can be determined by taking ToC measurements of E and L fluxes both inside (λ_{in}) and outside (λ_{out}) the O2A feature under use of the following system of equations [7]:

$$\begin{cases} L(\lambda_{\mathrm{in}}) = \frac{r(\lambda_{\mathrm{in}}) \cdot E(\lambda_{\mathrm{in}})}{\pi} + F(\lambda_{\mathrm{in}}) \\ L(\lambda_{\mathrm{out}}) = \frac{r(\lambda_{\mathrm{out}}) \cdot E(\lambda_{\mathrm{out}})}{\pi} + F(\lambda_{\mathrm{out}}) \end{cases} \tag{9}$$

With the further assumption that both r and F remain constant within the narrow retrieval range of the measurement **(A4)**, the system of equations can be resolved to yield the targeted retrieval principle [7]:

$$\begin{cases} r = \frac{L(\lambda_{\mathrm{out}}) - L(\lambda_{\mathrm{in}})}{E(\lambda_{\mathrm{out}}) - E(\lambda_{\mathrm{in}})} \cdot \pi \\ F = \frac{E(\lambda_{\mathrm{out}}) \cdot L(\lambda_{\mathrm{in}}) - L(\lambda_{\mathrm{out}}) \cdot E(\lambda_{\mathrm{in}})}{E(\lambda_{\mathrm{out}}) - E(\lambda_{\mathrm{in}})} \end{cases} \tag{10}$$

Throughout the derivation of equation (10), four key approximations were made: three related to the coupled atmosphere-vegetation RT **(A1-A3)** and one concerning the algorithm's methodology **(A4)**. Each of these simplifications could potentially introduce a retrieval artifact. As a consequence, radiance-based F retrievals using the ToC approach are susceptible to numerous errors. In the following section, a brief discussion on these simplifications and their implications for retrieval accuracy will be presented in the form of an error assessment.

2.2.1 Error 1: Surface Reflectance Anisotropy:

(A1): $$r_{so}(\Omega_s, \Omega_v, \lambda) \neq r_{do}(\Omega_v, \lambda)$$

The FLD method implicitly assumes a Lambertian surface reflectance [10], by setting the BRF (r_{so}) of the target equal to the HDRF (r_{do}). This assumption, however, is violated by the directional reflectance behavior of green vegetation, which exhibit Non-Lambertian scattering properties.

From Eq. (7) it is obvious that changing fractions of direct sunlight (E_{dir}) and diffuse skylight (E_{dif}) at the canopy surface yield different sensor scattered radiance, dependent from sun-target-observer geometries, even if the total surface E is perfectly known. The role of inter-pixel uncertainties in F retrievals arising from the surface reflectance anisotropy has not yet been finally answered.

Damm et al. [10] found very small errors in the range of 1% associated to the Lambertian assumption of basic FLD algorithms. In a modeling experiment from 2015, Damm et al. [11] reported differences in two reflectance indexes of up to 9% for the NDVI and up to 12% for the PRI when simple canopies were observed under either full or diffuse illumination. For F retrievals derived from 3FLD algorithm, however, no significant effect could be isolated. They concluded that F is less sensitive to reflectance anisotropy, at least for certain constellations of illumination-observation angles.

More recently, Liu et al. [36] linked different reflectance for direct and diffuse light arising from the BRDF characteristics of vegetation canopy to an in-filling effect (positive or negative) on the apparent reflectance within the O2A window.

2.2.2 Error 2: Atmospheric Effects

(A2): $\tau_\lambda^{atm} \neq 1 \quad , \quad L_\lambda^P \neq 0$

The FLD method implicitly ignores atmospheric effects by assuming that the path between the sensor and target can be neglected. However, the assumptions of an atmospheric transmittance close to one ($\tau_\lambda^{atm} \approx 1$) or a path scattered radiance close to zero ($L_\lambda^P \approx 0$) are violated when the atmospheric path length increases, as with a higher mount of sensors (e.g. on tower or airborne platforms) or with larger solar or view zenith angles (SZA, VZA) [36].
The upwelling radiance L measured from at a reference board above the canopy has travelled a longer distance through the atmosphere than the downwelling irradiance measured at the same height. The additional oyigen absorption will cause deeper absorption features in L than in E, which can offset the infilling by F in L [62]. At the same time, also the emitted F radiance is weakened by the upward transmittance of the atmosphere, which additionally intensifies the underestimation of fluorescence signal with higher sensor-target distance.
Sabater et al. [57], among others, demonstrated that even a few meters of atmosphere at sea level pressure can severely impact the accuracy of FLD based SIF retrievlas. To date, several methods to correct the additional deepening over the path from the sensor height to the surface ($E^{sensor} = E^{suface}/\tau_\downarrow$) and back to the sensor height ($L^{sensor} = L^{surface} \cdot \tau_\uparrow$) were developed and successfully tested [35, 57, 62]. However, because SIF is such a weak signal these methods require the precise knowledge of the atmospheric profile and other atmospheric parameters as input to achieve good results.

Furthermore, as the target-sensor distance increases, ToC retrievals that neglect the path scattered radiance (L_λ^P) may be affected by noise, leading to additional retrieval artifacts. This noise includes path radiance from sunlight scattered within the atmosphere that has not interacted with the target, as well as path radiance from objects outside the field of view (adjacency effect) [64].

2.2.3 Error 3: Surface Illumination

(A3): $\left(\frac{E_{dir}}{E_{dif}}\right)^{ToC} \neq \left(\frac{E_{dir}}{E_{dif}}\right)_{xy}^{Surf}$

The FLD method implicitly assumes a fully illuminated canopy in the sensor's FOV, by estimating the downwelling irradiance (E) from a reference board above the vegetation surface.
As highlighted in the introduction, the surface E field is not constant. The changing fractions of E_{sun} and E_{sky}, each with distinct absorption band depths after different atmospheric RT, can lead to pronounced infilling artifacts of F in L.
However, this perspective is a simplification of the actual scenario. Spectral changes around the O_2A feature are also influenced by canopy RT. While Eq.(7) provides a reasonable approximation of the sensor scattered L for homogeneous canopies, it is not adequate for more complex vegetation structures, such as forests on a high spatial resolution.
In reality, the radiative transfer in vertically structured canopies is extremely complex since reflected radiance L_R is not only determined by the first-order scattering which separates the sunlit and shaded components, but also multiple scattering after the first collision of light with foliage or the background [8, 31]. A beam of light can undergo several orders of scattering before it is totally absorbed or reflected back to space. The shaded components appear very dark when only the direct sunlight (E_{sun}) is faced, and slightly brighter when also the diffuse sky light ($E_{sky\downarrow}$) and the coupled backscattered diffuse upwelling flux from the atmosphere ($E_{sky\uparrow\downarrow}$) are considered (see Eq. (4-6)). Multiple scattering, on the other hand, provides an additional source of irradiance at the canopy surface, which can greatly increase the reflectivity of the shaded components [66]. While sunlit regions also experience these effects, their impact on radiative fluxes is less significant due to the predominant direct sunlight they receive [8]. As a result, an additional term is introduced to the surface irradiance budget, representing the multiple scattering contributions, expected to be dominated from GO-scattering, (E_{GO}). Consequently, Eq. (4) can be reformulated as:

$$E_{surface}(x, y, \lambda) = E_{sun} + E_{sky\downarrow} + E_{sky\uparrow\downarrow} + E_{GO}. \tag{11}$$

Of course, these multiple scattering contributions from surrounding elements (E_{GO}) are expected to be wavelength dependent and primarily controlled by the local canopy geometry and the vegetation optical properties. The role of the canopy RT (i.e., volumetric and geometric-optical scattering) on the formation of illumination artifacts remains unclear.

2.2.4 Error 4: Algorithm Methodology

(A4): $\left(\frac{dr}{d\lambda}\right) \neq constant \quad , \quad \left(\frac{dF}{d\lambda}\right) \neq constant$

The sFLD principle assumes that r and F fluxes remain constant across the entire absorption region, including adjacent reference wavelengths. This assumption, however, is violated by the spectral behavior of r and F in vegetation canopies [2]. Within the O_2A retrieval range, green vegetation typically exhibits a slight non-linear decrease in reflectance towards the red edge, while F emissions display a non-linear increase towards the far-red emission peaking at 740nm [7]. Over the years, various retrieval algorithms based on the FLD principle have been developed. Their primary distinction lies in how they address the non-linear changes of r and F near the absorption line.
Prior research has highlighted varying levels of uncertainties stemming from these distinct algorithmic methodologies. Moreover, the choice of reference bands and interpolation methods used in algorithms is a further source of uncertainty [7, 10].

2.2.5 Implications for the Modeling Experiment:

Combining the information from Chapters 2.1 and 2.2, it becomes evident that fluorescence retrievals using passive RS sensors are complex and multifaceted in their nature.
The apparent fluorescence signal retrieved by a radiance-based algorithm ($F_{retrieved}$) in a first order contain the sensor scattered fluorescence emission escaped from the surface pixel into the FOV of the sencor (F_{obs}=$F_{tot} \times f_{esc}$) and a bias-term ($\varepsilon_{\mathbf{tot}}$) which disturb the accuracy of the retrieval.

$$F_{\text{retrieved}}(E, L) = \underbrace{F_{\text{tot}}(\lambda_{in}) \times f^{esc}(\lambda_{in}, \Omega_v)}_{\text{Physiological Response}} \times (1 + \varepsilon_{tot}) \tag{12}$$

$$\varepsilon_{tot} = f(\underbrace{\varepsilon_{illumination}}_{\frac{E_{dir}}{E_{diff}} \neq const.}, \underbrace{\varepsilon_{anisotropy}}_{r_{so_\lambda} \neq r_{do_\lambda}}, \underbrace{\varepsilon_{atmosphere}}_{\substack{\tau_\lambda^{atm} \neq 1 \\ L_\lambda^P \neq 0}}, \underbrace{\varepsilon_{algorithm}}_{\substack{(\frac{dr}{d\lambda}) \neq const. \\ (\frac{dF}{d\lambda}) \neq const.}}, \underbrace{\varepsilon_{measurement}}_{\text{SR,SNR,SSI,...}}) \tag{13}$$

The overall bias ($\varepsilon_{\mathbf{tot}}$) is a composite function encompassing various individual biases that impact the SIF retrieval. Three major biases ($\varepsilon_{\mathbf{illumination}}$, $\varepsilon_{\mathbf{anisotropy}}$, $\varepsilon_{\mathbf{atmosphere}}$) stemming from simplifications regarding the coupled atmosphere-vegetation RT. They affect the accuracy of the retrieved signal mainly through alterations in the spectral signature of the measured upwelling (L) relative to the downwelling (E) fluxes, or vice versa, and hence, cause infilling artifacts. A further bias can result from the methodology of the algorithm itself ($\varepsilon_{\mathbf{algorithm}}$), specifically from the wrong assumption about the behavior of r and F within the small retrieval range. Furthermore, also measurement errors ($\varepsilon_{\mathbf{measurement}}$) mainly arising from unfavorable sensor characteristics (e.g. low signal to noise ratios in used bands) can significantly comprise to the overall retrieval bias.
Decoupling the total bias ($\varepsilon_{\mathbf{tot}}$) into its individual components is difficult, primarily due to the uncertainty of whether these biases are additive or multiplicative in relation to one another.
In terms of interpreting the illumination artifacts, a further complexity arises from the fact, that the truth fluorescence radiance is also expected to be highly sensitive to shadows (see Chapter 2.1).
With that in mind, the primarily objectives of this thesis include:

(i) Quantifying the illumination error (ε_{ill}) as well as its spatial and temporal dynamics in a representative virtual forest scene.
(ii) Exploring the impact of the canopy radiative transfer on the effect size of illumination artifacts.
(iii) Investigating the scale dependency of illumination uncertainties.

3 Method

3.1 Modelling Set-Up

As discussed in Chapter 2, a radiance-based SIF retrieval is a composition of the true fluorescence radiance scattered into the sensor and several error terms that biases the accuracy of the retrieved signal. The decoupling of the illumination error from the other error terms is not a trivial task but can be achieved by modelling all downwelling and upwelling radiative fluxes at several heights above the canopy:

- immediately at the surface layer of the canopy ($E^{Surface}$, $L_R^{Surface}$, $F^{Surface}$)
- at the top of canopy (E^{ToC}, L_R^{ToC}, F^{ToC})
- at a reference board above the canopy (E^{Sensor}, L_R^{Sensor}, F^{Sensor})

Figure 1 illustrates the principle of the modeling experiment. It relies on the fact that not all errors appear at the various measurement heights. Hence, by employing an algorithm with different combinations of E and L fluxes as input, individual errors can be seperated from one another, as explained in the further section.

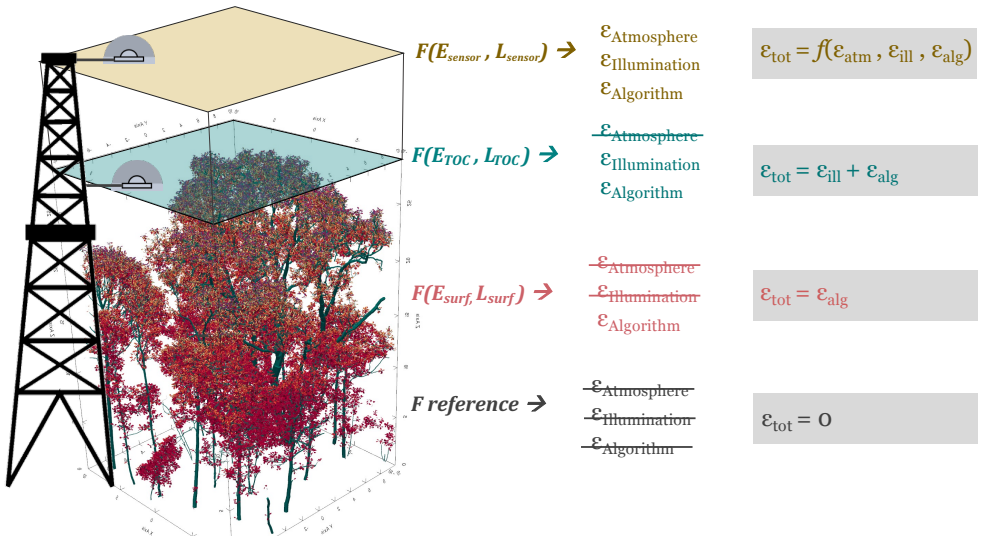

Figure 1: Principle of the modeling experiment

$\varepsilon_{\textbf{algorithm}}$: The difference between the truth fluorescence signal (F_{ref}) and the SIF retrieval using the accurate E and L fluxes immediately at the canopy surface layer $F(E_{surf}, L_{surf})$, can only be associated to the algorithm error which is caused by wrong assumptions of r and F within the retrieval range. Thus, the absolute relative error of the algorithm at a canopy element i can be calculated as:

$$|\varepsilon|_{alg,i} = \left| \frac{F(E_{surface}, L_{surface})_i - F_{ref_i}}{F_{ref_i}} \right| \tag{14}$$

$\varepsilon_{\textbf{illumination}}$: In real world applications the surface E field is unknown and fluxes were estimated above the vegetation body. As a consequence, the difference between the F retrieval using the wrong irradiance input immediately at the ToC $F(E_{ToC}, L_{ToC})$ and the F retrieval using the perfectly accurate radiative fluxes $F(E_{surface}, L_{surface})$ correspond to the illumination error and can be calculated as:

$$|\varepsilon|_{ill,i} = \left| \frac{F(E_{ToC}, L_{ToC})_i - F(E_{surface}, L_{surface})_i}{F(E_{surface}, L_{surface})_i} \right| \tag{15}$$

$\varepsilon_{\textbf{atmosphere}}$: With increasing target-sensor distance, atmospheric absorption and path scattered radiance can further disturb the accuracy of the retrievals. To separate the resulting atmospheric error from the illumination error, it can be quantified as the discrepancy between $F(E_{ToC}, L_{ToC})$ and the retrieval at a certain sensor level:

$$|\varepsilon|_{atm,i} = \left| \frac{F(E_{sensor}, L_{sensor})_i - F(E_{ToC}, L_{ToC})_i}{F(E_{ToC}, L_{ToC})_i} \right| \tag{16}$$

$\mathcal{E}_{\mathbf{anisotropy}}$: In this study all vegetation surfaces were treated as Lambertian surfaces, thus neglecting leaf specular reflectance and muting effects related to surface reflectance anisotropy on a leaf level. Moreover, the study focuses on nadir fluxes only and hence do not investigate potential anisotropy effects arising from the canopy BRDF characteristics.

$\mathcal{E}_{\mathbf{measurement}}$: Also, the measurement error was assumed to be zero. This assumption was based on the sufficient spectral sampling interval (SSI) and spectral resolution (SR) of the virtual sensor and the absence of signal to noise (SNR) variations, such as differing SNR values across different spectral bands, which are typical in real-world scenarios. However, the modeled output isn't completely noise-free. The path tracing algorithms used in the RT simulation introduce some level of Monte Carlo noise.

Moreover it is important to highlight that the provided modelling approach assumes additive nature for the individual biases. The decoupling of $\mathcal{E}_{\mathbf{alg}}$, $\mathcal{E}_{\mathbf{ill}}$ and $\mathcal{E}_{\mathbf{atm}}$ from the total retrieval bias ($\mathcal{E}_{\mathbf{tot}}$) can therefore only achieve accurate results if this requirement is fulfilled (see Figure 1). The relationship between the algorithm error and the illumination error was tested, revealing a high additive character between the two sub-biases ($\mathcal{E}_{\mathbf{tot}}^{\mathbf{ToC}} = \mathcal{E}_{\mathbf{alg}} + \mathcal{E}_{\mathbf{ill}}$) (see Appendix 1 for further details). Therefore, it can be expected that these two error sources can be separated with considerable precision.
The nature of the atmospheric error —whether additive or multiplicative— remains unclear since no sensor fluxes at higher altitudes were simulated. However, for the purposes of this study, the atmospheric error is not relevant as it falls outside the scope of the topic. Nonetheless, it warrants attention in future research.

3.2 Virtual Forest Scene

The Wytham Woods 3D V2 model [6] forms the basis of the modeling experiment, representing a one-hectare deciduous forest located in Wytham, UK. The forest is dominated by three species: Acer pseudoplatanus (Sycamore), Fraxinus excelsior (Ash) and Corylus avellana (Hazel). The mean annual temperature is 10°C, the mean annual rainfall is 726 mm and the mean annual radiation is 118 W/m2 [5]. Calders et al. [6] used highly detailed 3D terrestrial laser scanning (TLS) data to generate the realistic forest scene for purpose of RT model simulations. TLS data were matched with traditional census data to determine the species of each individual tree and allocate species-specific radiometric properties.

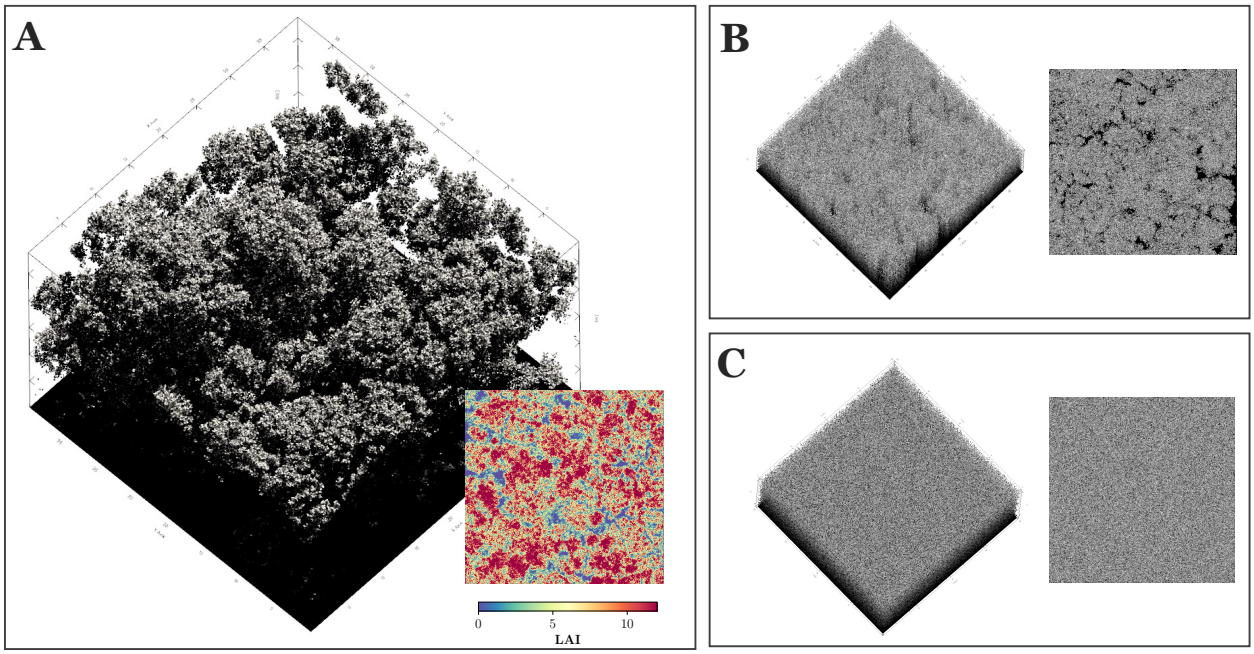

Figure 2: **(A)** Realistic virtual 3D forest scene and corresponding LAI map. **(B)** Vertically homogenized forest abstraction. **(C)** Fully homogenized forest abstraction (vertical and horizontal).

The virtual forest mock-up used in this study was partly obtained from the original Wytham 3D Model and encompasses a size of 40x40m. The sloped terrain model of the original scene was rejected, and all used trees have been shifted along the z-axes to lay on a common flat surface. This guarantees continuity and

energy-conservation on the DART scene boundaries and facilitates the spatial comparability of pixelwise simulated radiative fluxes on different heights (Surface, ToC, Sensor). In addition, the scene has been cropped to fit the 40x40m bounding-box. To do so, any primitive (triangle, cylinder or disc) laying outside the new box has been omitted and leaf triangles that exceeded the boundary by less than 50% were integrated into the scene with the same leaf area and orientation by moving along the x-y axis. All tree stems and branches represented as closed 3D cylinders were excluded from the scene.
The resulting 40x40m forest transect contains 85 individual canopies with a total number of 554'144 leaves represented by two triangles each (tetragons). Leaf area results from a uniform leaf size distribution (LSD) and span areas between 0.009m2 to 0.015m2.
The final scene portrays a densely vegetated forest during the peak of the growing season, characterized by an average Leaf Area Index (LAI) of 8.2 and a nadir gap fraction of 15.2%. The individual crown heights varying from 2m for young understory vegetation to a maximum of 29m, resulting in a dynamic and heterogeneous canopy surface with pronounced vertical and horizontal variation.

To investigate the impact of the horizontal and vertical heterogeneity on SIF retrieval uncertainties, the realistic 3D forest scene was divided into two representations with simpler levels of structural complexity:

(i) **Vertical homogenization:** In a first additional mock-up, the 3D scene was vertically homogenized, resulting in a cube of leaves with horizontal variation in the structural parameters (e.g., LAI, nadir gap fraction) but without canopy vertical heterogeneity. To do so, the forest section was divided into 25'600 vertical columns of the size 0.25mx0.25m. All leaves within a column were then normalized between 0m and 17.4m which represents the mean canopy height of the original scene.

(ii) **Vertical and horizontal homogenization**: In a second additional mock-up, the forest scene was fully homogenized (both vertically and horizontally). To do so, all leaves of the initial scene were randomly redistributed in a 40mx40mx17.4m cube. The resulting mock-up do not have any spatial variations in the structural parameters anymore.

Figure 2 illustrates the 3D forest mock-up and its vertically and fully homogenized abstractions. All scenes contain the identical set of leaves and differ only in their spatial distribution within the 3D volume.

3.3 DART Model

The work presented in this study was carried out with DART model Version 5.8.12 [19]. DART is one of the most comprehensive and accurate 3D radiative transfer models and has been continuously developed and improved since 1992. It has been successfully cross compared with other state of the art RTMs, demonstrating its accuracy for both schematic and realistic canopy scenarios during the RAMI3 [70] and RAMI4 [69] experiments.
DART produces RS images of natural and urban landscapes at any sensor level and over the entire optical domain (UV, VIS, NIR, TIR). Additionally, DART computes the quantitative 3D radiative budget (i.e., intercepted, absorbed, reflected, and emitted radiation) for each geometric surface in a scene separately and is adapted to any experimental (e.g., atmosphere, sun direction) and instrumental (e.g., viewing direction, altitude, spatial and spectral resolutions) configuration [17].
In 2017 the leaf radiative transfer model Fluspect-Cx was embedded in the DART environment which enables the modelling of forward and backward fluorescence radiance [18]. The couplet atmosphere-earth radiative transfer follows a flux tracking approach. The standard flux tracking mode, DART-FT, uses an adapted forward discrete ordinates method. This mode iteratively tracks radiation in user-defined discrete directions [67]. Recently, DART-Lux mode was implemented to improve efficiency in the earth scene module. It uses an unbiased and fast bidirectional path tracing (BDPT) algorithm that significantly reduces computing time and memory requirements to simulate images of large and complex landscapes. The BDPT algorithm constructs paths that initiate both from the sensor and light sources and solves the rendering equation [26] at any position in the earth scene grid by using Monte Carlo integration [68].

3.3.1 Modelling of Radiative Fluxes

As discussed in Chapter 3.1, the complete separation of the illumination error ($\varepsilon_{\mathbf{ill}}$) from the total retrieval bias ($\varepsilon_{\mathbf{tot}}$) of a radiance-based SIF retrieval requires the pixelwise modeling of E and L_R fluxes at two distinct heights (Surface and ToC).
Most remote sensing platforms measure upwelling radiance at an inclined sensor zenith angle (e.g., Tower

set-up: 20°-25°). Although DART offers the possibility to create RS images for any desired view angle and sensor configuration, in this study, nadir orthoimages were chosen as the primary output to ensure the highest level of pixelwise comparability among the data.

Modelling of ToC fluxes: The downwelling irradiance (E) reaching a ToC-pixel (x,y) at height z is modelled as the sum of all stored DART radiance fluxes ($L\downarrow_z$) integrated over the whole upper hemisphere, including the direct light from the sun direction $E^{dir}_{\downarrow z}(\theta_s, \phi_s)$ as well as the downwelling diffuse sky radiation $E^{dif}_{\downarrow z}$ and backscattered diffuse upwelling radiance $E^{coupl}_{\downarrow z}$ from any direction of the hemisphere ($\theta : [0, 2\pi], \phi : [0, \frac{\pi}{2}]$).

$$E_{\downarrow z}(x, y, \lambda) = E^{dir}_{\downarrow z} + E^{diff}_{\downarrow z} + E^{coupl}_{\downarrow z} = \int_0^{2\pi} \int_0^{\frac{\pi}{2}} L_{\downarrow z}(x, y, \lambda, \theta, \phi,) \cos(\theta) \sin(\theta)\, d\theta\, d\phi \tag{17}$$

Since the modelling of radiation propagation (incl. absorption and scattering) using an infitesimal number of directions would require a massive computational effort, DART discretize the 4π space into N directions summing up the contributions of downwelling radiance $L_{\downarrow z}(\theta_i, \phi_j)$ from each discrete angle pair as [17]:

$$E_{\downarrow z}(x, y, \lambda) \approx \sum_{i=1}^{N_\theta} \sum_{j=1}^{N_\phi} L_{\downarrow z}(x, y, \lambda, \theta_i, \phi_j) \cos(\theta_i)\, \Delta\omega \tag{18}$$

, where $N\theta$, $N\phi$ represent the number of discrete zenith (θ_i) and azimuth (ϕ_j) angels and $\Delta\omega$ the corresponding solid angle element. The accuracy of the approximation depends on the choice of the discrete angles and the sampling density, which is why DART offers the possibility to oversample specific regions of interest in the 4π space (e.g., hot-spot region).

In order to create orthoimages of the upwelling reflected and emitted radiance, DART stores each radiative flux $\Phi_v(x, y, z_i, \theta_v, \phi_v)$ that exits the vertical column (x,y) at a certain altitude after a finite number of scattering events. The specific radiance value of an orthoimage pixel x,y for any view direction (θ_v, ϕ_v) is given by (adapted from Schneider et al. [59]):

$$L_{\uparrow z}(x, y, \lambda, \theta_v, \phi_v) = \frac{\sum_i \Phi_v(x, y, z_i, \lambda, \theta_v, \phi_v)}{A_{xy} \cdot \cos(\theta_v) \cdot \omega_v} \tag{19}$$

, where $\sum_i \Phi_v(x, y, z_i, \lambda, \theta_v, \phi_v)$ is the sum of all DART fluxes leaving the column (x,y) reaching the vertical location z_i (TOC or Senor level), A_{xy} is the area of pixel (x,y) and ω_v is the solid angle associated to the nadir direction (θ_v, ϕ_v).
The coupling of the atmosphere RT (DART-FT) and the Earth scene radiative transfer (DART-LUX) happens in multiple steps using several transfer functions. More details can be found in Wang et al.,(2021) [67].

Modelling of surface fluxes: While 2D orthoimages of TOC radiometric properties can be directly extracted from DART-BRF product, DART lacks the capability to directly simulate nadir orthoimages of surface fluxes due to the different surface heights of the vegetation body along the pixels. Nevertheless, 2D images of surface fluxes can be derived from the 3D radiative budgets i.e., from the interception and scattering matrices by selecting all triangles forming the surface as viewed from nadir.
Unfortunately, it is important to note that simulating 3D radiative budgets can be computationally demanding, especially when dealing with large mock-ups at high spatial and spectral resolutions, as employed in this study. Consequently, certain simplifications were made to calculate surface irradiance in the absence of direct 3D simulations. $L_{surface}$ was approximated with L_{TOC} under the assumption that the path scattered radiance into the nadir direction is negligible ($L_p \approx 0$) and the upwelling transmittance is close to one ($\tau_\uparrow \approx 1$) for the short distances between an individual canopy surface element and the TOC layer. Furthermore, it was considered that radiance transmitted from deeper vegetation layers could be disregarded. For the entire forest environment, each individual surface was treated as a Lambertian scatterer with the same optical properties, i.e., reflectance (R) and transmittance (τ). This ensures to estimate the surface irradiance ($E_{surface}$) at a pixel (x,y) from the nadir scattered upwelling radiance at TOC as:

$$E_{\downarrow s}(x, y, \lambda) = E^{dir}_{\downarrow s} + E^{diff}_{\downarrow s} + E^{coupl}_{\downarrow s} + E^{GO}_{\downarrow s} = \frac{L_{TOC}(x, y, \lambda, \theta_v, \phi_v) \cdot \pi}{R(x, y, \lambda)} \tag{20}$$

, where $E^{GO}_{\downarrow s}$ represents the additional irradiance at a canopy surface element arising from multiple scattering and $R_{xy\lambda}$ is the leaf reflectance at a given pixel (x,y) and wavelength (λ).

In this study the accurate $E_{surface}$ derived from DART 3D radiative budget was used for the analysis of the vegetation RT, while the approxiamted E_{surf} was used in the spatio-temporal analyses to calculate the algorithm error ($\varepsilon_{\mathbf{alg}}$).

Modelling of fluorescence radiance: DART simulates leaf fluorescence emission (i.e., leaf backward/forward SIF of PSI and PSII) with the embedded FluspectCX model [65] as the product of (1) an excitation-emission matrix (M_{uv}) which contains Fluspect biochemical variables and fluorescence quantum yields (Φ_F) and (2) an irradiance matrix E_{leaf} which contains the leaf intercepted irradiance at any facet (i) of the 3D object file [17]:

$$Fs_{v,\mathrm{i}} = M_{uv,\mathrm{i}} \times E_{u,\mathrm{i}} \tag{21}$$

, where u denotes to the excitation bands and v to the emission bands. Afterwards, DART upscales leaf-level SIF to canopy SIF by using the bi-directional flux tracking method, which tracks SIF fluxes until being totally re-absorbed or escaped from the canopy in specified discrete directions, analogously to Eq.(19). Leaf biochemical and structural inputs as well as fluorescence quantum efficiencies (Φ_F) can be set either for individual foliage facets or as general parameters for all leaves or specific leaf groups (e.g., sunlit and shaded).

3.3.2 DART Parametrization

Radiative Transfer: All DART computations were run on the fully coupled atmosphere-vegetation bi-directional flux-tracking mode (DART-LUX) with the solar radiation (E_{sun}) and diffuse sky radiation (E_{sky}) as only light sources. DART can be used with standard gas and aerosol models as contained in the MODTRAN model [31]. In this study, the midlatitude summer gas model and the rural aerosol model with a visibility of 23 km were applied on each simulation. Moreover, DART offers the possibility to calculate the RT with or without air in the earth scene (fluid until ToC or until ground). Although the high computational effort, the mode including air in the scene was chosen, to track the oxygen absorption during multiple scattering in the canopy, where additional deepening of the ABD can occur. The Canopy radiative transfer was modeled with 100 discrete scattering directions in the whole 4π space, without oversampling the hot-spot up- and downward directions. The vegetation voxel grid was not filled with turbid media but with leaf triangles of the 3D forest scene (i.e., its structural abstractions).
Temporal Resolution: For every mock-up a complete daily cycle under clear sky conditions was modelled from 8:00 AM to 7:00 PM with an hourly sampling rate. Sun zenith angles (SZA) and sun azimuth angles (SAA) represent the 27. Juni 2023 at location of Wytham Forest near Oxford, UK (57.771°N, -1.3354°E).
Spatial resolution: Nadir orthoimages of radiative fluxes were simulated on a voxel grid of 0.04m (i.e., 1e6 pixel within the 40mx40m scene), with a scattering order of 100 (i.e., finite number of scattering events between photons and canopy elements). The high spatial resolution and scattering order is necessarily to catch fine scaled shadow dynamics (at the leaf level) and investigate the influence of volumetric- and geometric-optical scattering within the canopy during the couplet RT.
Spectral resolution: E and L_R fluxes around the O_2A absorption feature were modelled between 754-775nm with a spectral sampling interval (SSI) of 0.35nm (i.e., 61 spectral bands) and spectral resolution (SR) of 0.35nm. F fluxes were simulated based on 91 excitation and emission bands in the spectral region from 400 to 850 nm. A coarser sampling interval of 5nm was used since computational effort of F simulation increases to the power of used bands. Fluorescence radiance was then linearly interpolated within the O_2A spectral range.
Optical properties: Each leaf within the mock-up was treated with the same optical properties with both sides participating in the radiative transfer process, including fluorescence emissions. Moreover, Lambertian scattering was assumed for each vegetation surface (triangle). Leaf reflectance (r) and transmittance (τ) were derived from in-situ data provided by Calders et al. [6] and implemented as the average leaf spectra of the seven most abundant species in the Wytham forest. The top surface of ground pixels was characterized using the same vegetation optical properties, whereas the underlying soil was defined by the average soil spectra from the dataset provided by Calders et al. [6].
Fluorescence emissions were simulated using a unified approach, considering PSI and PSII as a single photosystem with a constant quantum efficiency of 0.012 (i.e., no distinctions of fluorescence yield between sulit and shades leaves were made). FluespectCX pigment parameters (i.e., leaf chlorophyll $a+b$, total carotenoid and brown pigment contents) were adapted from fresh leaf measurements by Calders et al. [6] in the Wytham forest study site. For unknown FluespectCX parameters default values from DART were used.
Uniform optical properties and a constant fluorescence yield along all leaves ensure that variations in F retrievals across different scales and canopy regions primarily reflect the impact of shadows, minimizing potential confounding effects from factors like leaf biochemistry or other optical properties.

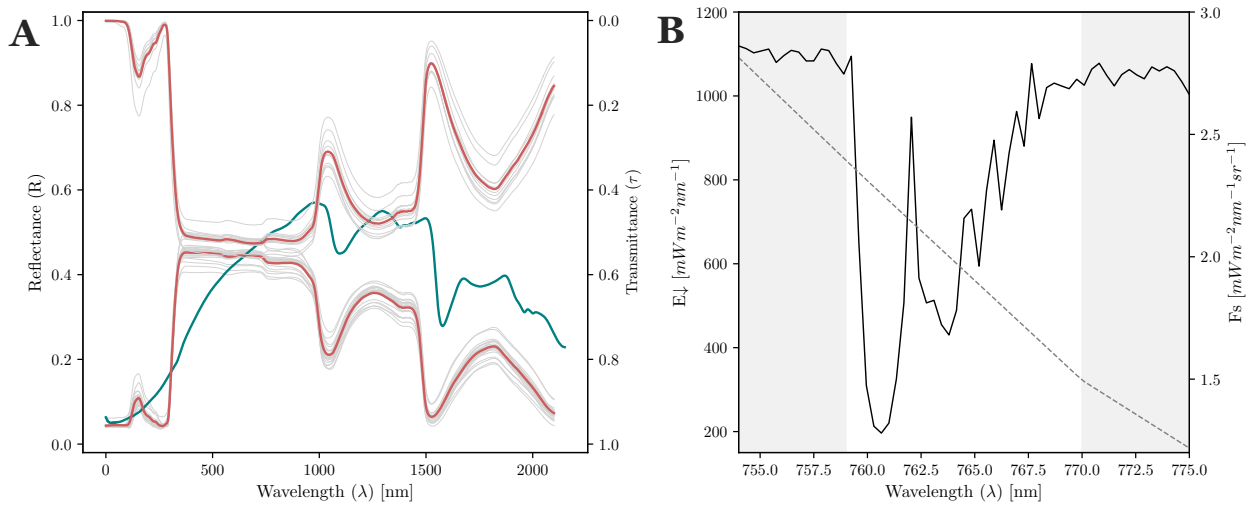

Figure 3: **(A)** Leaf optical properties: leaf reflectance (r_{leaf}) and leaf transmittance (τ_{leaf}) shown as red lines. Soil reflectance is represented by the green line. **(B)** Spectral resolution of the modeled O_2A feature using 61 bands between 754nm and 775nm (solid line). Grey areas indicate the left and right reference shoulders. Fluorescence emission within the O_2A feature is shown as a dashed line.

3.4 Implementation of Radiance-Based SIF Algorithms:

In total, three radiance-based algorithms were applied to retrieve far-red SIF in the O_2A absorption feature. Each algorithm exhibited a unique level of complexity and made specific assumptions tailored to its retrieval methodology.
The region significantly affected by O_2 absorption was defined between 759nm and 770nm, with a local minimum observed at 760.65nm. Consequently, all spectral bands located beyond the O_2A feature can be considered as left and right shoulders of the absorption region.

3.4.1 sFLD Algorithm:

The sFLD method [49] requires only one measurement of downwelling E and upwelling L inside and outside the absorption feature to estimate chlorophyll fluorescence. It was pixel-wise implemented as followed [10]:

$$F(\lambda_{\text{in}}) = \frac{E_{\downarrow}(\lambda_{\text{out}}) \cdot L_{\uparrow}(\lambda_{\text{in}}) - L_{\uparrow}(\lambda_{\text{out}}) \cdot E_{\downarrow}(\lambda_{\text{in}})}{E_{\downarrow}(\lambda_{\text{out}}) - E_{\downarrow}(\lambda_{\text{in}})} \tag{22}$$

, where λ_{in} denotes the spectral band with the smallest $E_{\downarrow}$ value within O_2A feature (i.e. where oxygen absorption is most pronounced), and λ_{out} represents the wavelength of the left reference shoulder where $E_{\downarrow}$ reaches its local maxima ($\lambda_{out} \in [754nm, 759nm]$).
The primary limitation of this algorithm stems from its assumption of constant values for r and F across the retrieval range.

3.4.2 3FLD Algorithm:

The 3FLD method [40] accounts for a linear variation of r and F over the investigated spectral range and uses both shoulders to calculate a linearly interpolated virtual reference band. Therefore, Eq.(22) can be rewritten as [10]:

$$F(\lambda_{\text{in}}) = \frac{(w_r \cdot E_{\downarrow}(\lambda_r) + w_l \cdot E_{\downarrow}(\lambda_l)) \cdot L_{\uparrow}(\lambda_{\text{in}}) - (w_r \cdot L_{\uparrow}(\lambda_r) + w_l \cdot L_{\uparrow}(\lambda_l)) \cdot E_{\downarrow}(\lambda_{\text{in}})}{(w_r \cdot E_{\downarrow}(\lambda_r) + w_l \cdot E_{\downarrow}(\lambda_l)) - E_{\downarrow}(\lambda_{\text{in}})} \tag{23}$$

$$\text{, where} \quad w_r = \frac{\lambda_r - \lambda_{in}}{\lambda_r - \lambda_l}, \quad \text{and} \quad w_l = \frac{\lambda_{in} - \lambda_l}{\lambda_r - \lambda_l} \tag{24}$$

λ_{in} represents the minimum band within the absorption feature ($\lambda_{in} = 760.65nm$), while λ_l and λ_r correspond to the maximum bands on the left and right shoulders, respectively. Later, were linearly interpolated by the

weights w_l and w_r to account for the varying distances between the two shoulder bands (λ_l, λ_r) to the retrieval band λ_{in}.
The proposed improvement in the 3FLD method aims to enhance accuracy beyond that of the standard sFLD. However, the spectral characteristics of the O_2A feature require the selection of the second reference wavelength considerably distant from the maximum absorption line ($\lambda_r > 770nm$). This extension increases the investigated retrieval range by roughly 2/3 compared to sFLD method.

3.4.3 iFLD Algorithm:

In order to calculate F with the iFLD method [2] the full spectral information of downwelling irradiance E and upwelling radiance L across the 61 bands was utilized to compute two correction factors, $\hat{\alpha_R}$ and $\hat{\alpha_F}$. These factors account for the non-linear variations in both reflectance R and fluorescence F fluxes within the considered wavelength range and the FLD principle adapts to the followed equation [7]:

$$F(\lambda_{\text{in}}) = \frac{\hat{\alpha}R \cdot E_{\downarrow}(\lambda_{\text{out}}) \cdot L_{\uparrow}(\lambda_{\text{in}}) - L_{\uparrow}(\lambda_{\text{out}}) \cdot E_{\downarrow}(\lambda_{\text{in}})}{\hat{\alpha}R \cdot E_{\downarrow}(\lambda_{\text{out}}) - \hat{\alpha}F \cdot E_{\downarrow}(\lambda_{\text{in}})} \tag{25}$$

The approach assumes that the actual reflectance R closely resembles the apparent reflectance R_{app} after removing the peak caused by the infilling of fluorescence F. To interpolate R_{app} within the O_2A feature, the study uses the wavelengths of all local radiance maxima of the left shoulder ($\lambda_{l,max,i} \in [754nm, 759nm]$) and right shoulder ($\lambda_{r,max,i} \in [770nm, 775nm]$) through cubic spline interpolation. Subsequently, pixelwise correction factors $\tilde{R}_{\text{app}}$ are computed according to the equation [7]:

$$\hat{\alpha}_R = \frac{R_{\text{app}}(\lambda_{\text{out}})}{\tilde{R}_{\text{app}}(\lambda_{\text{in}})} \tag{26}$$

, where $\tilde{R}_{app}(\lambda_{in})$ represents the reflectance value at 760.65nm of the peak-removed R curve, and $R_{app}(\lambda_{out})$ is the reflectance value of the left shoulder reference band in a given pixel.
Analogously, the correction factor accounting for the nonlinear characteristics of F can be calculated as [7]:

$$\hat{\alpha}_F \approx \frac{E_{\downarrow}(\lambda_{\text{out}})}{\tilde{E}_{\downarrow}(\lambda_{\text{in}})} \cdot \hat{\alpha}_R \tag{27}$$

, where $\tilde{R}_{\downarrow}(\lambda_{in})$ is obtained by interpolation of the irradiance in order to predict E↓ unaffected by atmospheric absorption. In contrast to $\tilde{R}_{app}(\lambda_{in})$ it was interpolated with a 2^{nd} order polynom, as suggested by Cendrero et al. [7].

3.5 Modelling of Shadow-Fraction (fSh):

The shadow fraction (fSh) as seen form nadir is an important parameter since illumination artifacts are expected to be highly sensitive to changing fractions of E_{dir} and E_{dif} at the canopy surface.
Given that shadow characteristics vary with wavelength, this study specifically defines 'shadow' in relation to the 758nm wavelength in the NIR range. This particular wavelength signifies a local maxima on the left shoulder of the O2A band.

Method: The used modeling approach, calculates fSh from the 2D surface irradiance maps in a classical sense. Pixels which did not received any direct light ($E^{dir,758}_{\text{surface}} = 0$) were treated as fully shaded (umbra, shelf-shadow). Pixels that received the same or higher amount of direct light as measured above the canopy ($E^{dir,758}_{\text{ToC}}$) were treated as fully illuminated (sunlit). Pixels in the range between were linearly normalized and treated as partly shaded (penumbra).

$$\begin{cases} E^{dir}_{\text{surface}} = 0 & f\text{Sh} = 1 \\ E^{dir}_{\text{ToC}} > E^{dir}_{\text{surface}} > 0 & f\text{Sh} = \text{Normalized [0,1]} \\ E^{dir}_{\text{surface}} \geq E^{dir}_{\text{ToC}} & f\text{Sh} = 0 \end{cases} \tag{28}$$

4 Results

The results section of this study is divided into three parts. The first part examines the temporal and spatial dynamics of the algorithm error and the illumination error at the leaf-level (Chapter 4.1). The second part investigates the underlying canopy radiative transfer, with a focus on explaining the spatio-temporal trends detected in section one (Chapter 4.2). Finally, the third part scales up the remote sensing fluxes to the canopy and ecosystem levels, assessing the impact of sensor footprint on illumination artifacts (Chapter 4.3).

4.1 Dynamics of the Illumination Error at High Spatial Resolution:

In general, algorithm errors ($\mathcal{E}_{algorithm}$) (caused by wrong assumptions of R and F within the retrieval range) were found to be one order of magnitude smaller than illumination errors ($\mathcal{E}_{illumination}$) (caused by wrong irradiance input). On average, both errors exhibited variation throughout the day, reaching their peaks at midday when SZA is low (see Figure 4A, red curve: $\mathcal{E}^{3FLD}_{algorithm}$, bluish curves $\mathcal{E}^{3FLD}_{illumination}$).

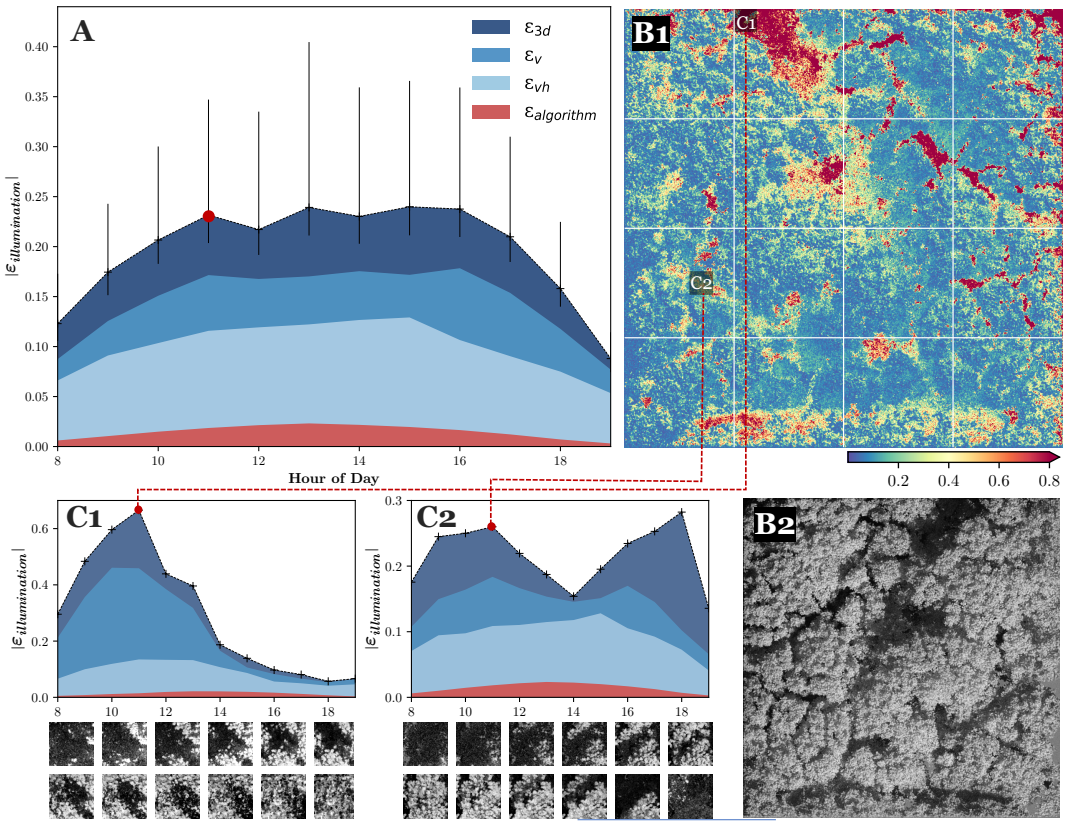

Figure 4: **(A)** Temporal trends of algorithm error (red) versus illumination error (blueish colors), further broken down into contributions from the 3D forest (ε_{3D}), its vertically homogenized abstraction (ε_v), and the fully homogenized abstraction (vertical and horizontal, ε_{vh}). Error bars represent a third of 95% quantiles (Q_{95}), highlighting the strong variability around the mean. **(B1,B2)** Spatial illumination error patterns at 11AM and the corresponding monochromatic surface irradiance image at $\lambda = 758nm$. **(C1,C2)** Temporal error trends for two $4m^2$ subsections. (Please not that this Figure correspond to retrievals with the 3FLD algorithm.)

Algorithm Error: Despite the temporal variations (i.e., dependency on SZA), algorithm errors ($\mathcal{E}^{sFLD}_{algorithm}$: 1-4%, $\mathcal{E}^{3FLD}_{algorithm}$: 0.5-3%, $\mathcal{E}^{iFLD}_{algorithm}$: 0.1-0.5%), were found to be spatially invariant (same error magnitude under shaded and sunlit conditions), independent of measurement scale (i.e., FOV of sensor) and almost independent of the structural complexity (i.e., same error for 3D-mock-up, vertical homogenized-, and fully homogenized forest abstractions). Moreover, the impact of the algorithm error on the overall retrieval uncertainty remained low across all algorithms under examination. However, adjusting the assumptions about r and F within the retrieval range notably improved the accuracy of the algorithms, leading to the error sequence iFLD < 3FLD < sFLD.

Illumination Error: In contrast, illumination error ($\mathcal{E}_{illumination}$) was found to be highly dynamic in space (Figure 4B), time (Figure 4A) and showed significant sensitivity on the structural complexity of the vegetation surface (Figure 4A, blueish fields).

(i) Temporal dynamics: Much like the algorithm error, the illumination error typically exhibits a bell-shaped pattern throughout the day. The scene-averaged errors fluctuate between 10% and 23%, depending on the time of day. Consequently, the degree of illumination uncertainty is inversely related to the overall presence of shadows in the forest scene. As depicted in Figure 5A, the portion of fully shaded area ($E_{dir} = 0$) diminishes from roughly 34% during the morning and evening to 19% at midday. When accounting for both fully shaded areas and partial shade (penumbra), the daily shadow cycle spans from 68% to 51%. It appears paradoxical that the illumination uncertainty, on average, reaches its peak impact during the time of day when shadow spread is minimal. However, it is important to recognize that not only shadow fractions are variable during the day. The DART simulation revealed that the spectral characteristics of downwelling direct and diffuse irradiance that enters the canopy also exhibit discernible daily variations (under clear sky conditions). As illustrated in Figure 5B, the relative O_2A absorption band depth shows distinct variation between sun and sky light that reaches its maximum difference at noon ($\Delta ABD_{|diffuse-direct|} = 1.6\%$). Consequently, shadows occurring around midday have a much higher error potential. Moreover, it was found that the ratio of direct to diffuse light reaching the ground increases with lower SZA (see Figure 5C). Therefore, the blocking of direct light at midday creates stronger contrasts between surface ABD relative to the measurement at ToC ($\Delta ABD_{|surface-ToC|}$). It seems that the average potential to produce illumination artefacts is not constant in time and mainly driven by the atmosphere RT.

However, Figure 4C indicate that when leaving the scene average and look at specific regions within the forest, the temporal shape can strongly deviate from the bell shaped curve, dependent on the local illumination condition on the ground. In example C1 the error peak appears in the morning due to the popping up of a shadow gap. Example C2 demonstrates a scenario where, instead of a peak, an error dip can be observed around noon. In such cases, the largest spectral difference between E_{sun} and E_{sky} still occurs at noon. However, the local configuration of the vegetation's surface results in minimal shadowing, which prevents a significant obstruction of direct light.

The strong influence of fractional shadow fields on the formation of illumination artefacts was also confirmed in the analysis of the structural complexity. By dividing the total illumination error into its structural contributions, it was found that on average, 30% of the error is induced by the vertical heterogeneity within the scene, another 20% can be attributed to the horizontal heterogeneity while the major part of roughly 50% is also present in the fully homogenized forest abstraction where self- and cast-shadows at the leaf level is the only source of shade (see Figure 1A, blueish curves). The fact, that the reduction of structural complexity under the same illumination conditions (and atmospheric RT) led to a significant decrease in the retrieval uncertainty, indicates the structural complexity as a main driver that controls the types and fractions of shadow present at a given location and sun geometry.

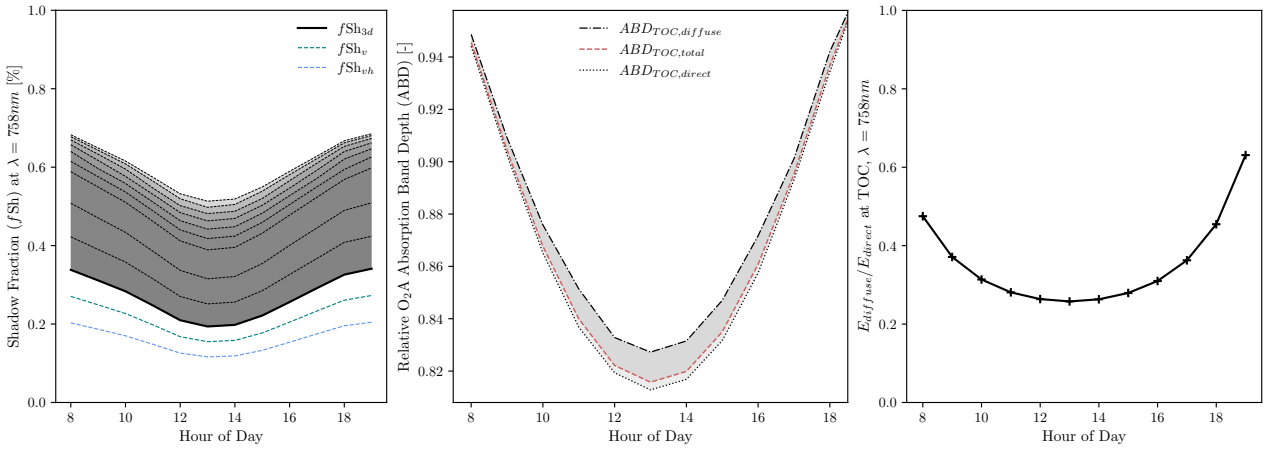

Figure 5: (A) Temporal dynamics of the overall shadow fraction (fSh). The solid black line correspond to the full shadow fraction in the forest scene ($E_{dir} = 0$), while the dashed black lines highlight the effects of partial shading (penumbra). Green and blue curves represent the fully shaded fractions in the vertically and fully homogenized forest versions, respectively. **(B)** Absorption band depth (ABD) of the O_2A feature for direct, diffuse, and total incoming irradiance at the ToC (E_{ToC}). **(C)** Ratio of diffuse to direct incoming light at the ToC (E_{dif}/E_{dir}).

(ii) Spatial dynamics: If we fix the time and take a closer look at the spatial distribution of the illumination error, large local variability was found ranging from almost 0 to far beyond 100% (see Figure 4B, 4A, representing the error distribution at 11 AM and 15 PM respectively). In general, small errors are detected over well-illuminated surfaces and high uncertainties occur in pronounced shadows. But even in fully shaded structures ($E^{dir}_{surface} = 0$) the illumination error showed large internal variability, assuming complex underlying canopy RT further discussed in Chapter 4.2.
When examining the direction of the error (rather than absolute errors), Figure 6 highlights a marked underestimation of true fluorescence emission in shaded conditions and a minor overestimation of F in sunlit areas.

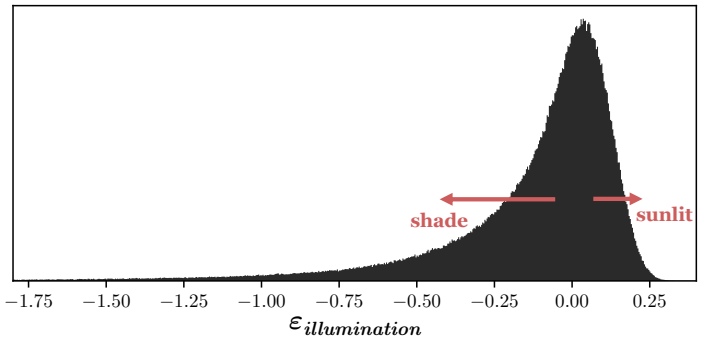

Figure 6: Distribution of illumination errors at 11AM, illustrated using the 3FLD fluorescence retrieval in the 3D virtual forest mock-up. Sample size: $N = 1 \times 10^6$ Pixels.

Figure 7A shows a random 4x40m transect through the forest and its abstracted versions. The transect contains three prominent shadow patterns, each varying in its vertical and horizontal configuration, as highlighted by the transparent grey bars.
The initial curve demonstrates how fluorescence emission reacts to changes in shadow fractions (fSh). As expected, the SIF radiance decreases notably in the presence of shadow, reflecting a physiological response to reduced PAR (from 2.8 to 0.7 mW $m^{-2}nm^{-1}sr^{-1}$). At the same positions, all evaluated algorithms exhibit a consistent trend: an escalation in uncertainty over shaded areas (reaching up to 110%) and a consistent base-uncertainty over well-lit patterns (10-20%). Although SIF emissions and illumination errors stem from separate processes (namely, ΔPAR and $\Delta ABD_{|surf-TOC|}$), both display a pronounced correlation with the varying light conditions in the surface E field.
With the removal of vertical heterogeneity (ε_v), the retrieval artefacts of the two left-handed shadow gaps almost completely disappeared while the feature on the right-hand side still produces a large retrieval artefact. It seems that the error potential of some geometric structures can be driven by either vertical, horizontal, or both types of heterogeneity.
With the removal of both, the vertical and horizontal (ε_{vh}) structure, the error signal drops down to a spatial invariant ground uncertainty driven by the cast-and self-shadows on the leaf level (dominated by volumetric scattering). When comparing the individual algorithms, it is noticeable that the sFLD algorithm generally exhibits a lower sensitivity to strong shading but shows higher effect sizes under well-illuminated conditions. Overall, the curves in Figure 7A confirm that although the temporal variation of the illumination error is mostly controlled by the atmosphere radiative transfer, at a fixed time, errors in a first order are following the shadow patterns.
(iii) Spatial resolution: However, to make conclusions about the effect size and dynamics of illumination artefacts for different remote sensing platforms, one must be aware that most retrieval-setups rarely track fluorescence emissions at such high spatial resolution. Figure 7B thus illustrates the influence of retrieval footprint on $\varepsilon_{illumination}$ at the example of a $12m^2$ area within the transect (see dotted red square).
Scanning the area at the full 4x4cm resolution (120x120 pixels) as it could be measured by a spectral imaging platform (e.g., SPECIM) results in a notably higher average absolute illumination uncertainty compared to treating the same area as a single pixel of $12m^2$, which would be the typical FOV of a conical non-imaging spectroradiometer in a conventional tower-based retrieval setup (e.g., FLOX).
The resolution dependent reduction of $\varepsilon_{illumination}$ counts 30% at the peak occurrence of the shadow gap (3PM) but is not equally for different day times or abstraction levels. It seems that increasing the retrieval footprint smooths local illumination conditions and reduces the occurrence of illumination extremes, resulting in a strong scale dependency that is further analyzed in Chapter 3.2.

When comparing the daily patterns of fluorescence with its retrieval, it becomes evident that the presence of the shadow gap significantly reduces the SIF signal ($PAR \downarrow$). Simultaneously, the retrieval process becomes less accurate ($\Delta ABD \uparrow$). As a result, the illumination error overlays the physiological response of SIF to shadow, leading to a further underestimation of the already reduced SIF signal. Moreover, variations in the surface E also impacts the accuracy of apparent reflectance (R_{app}).

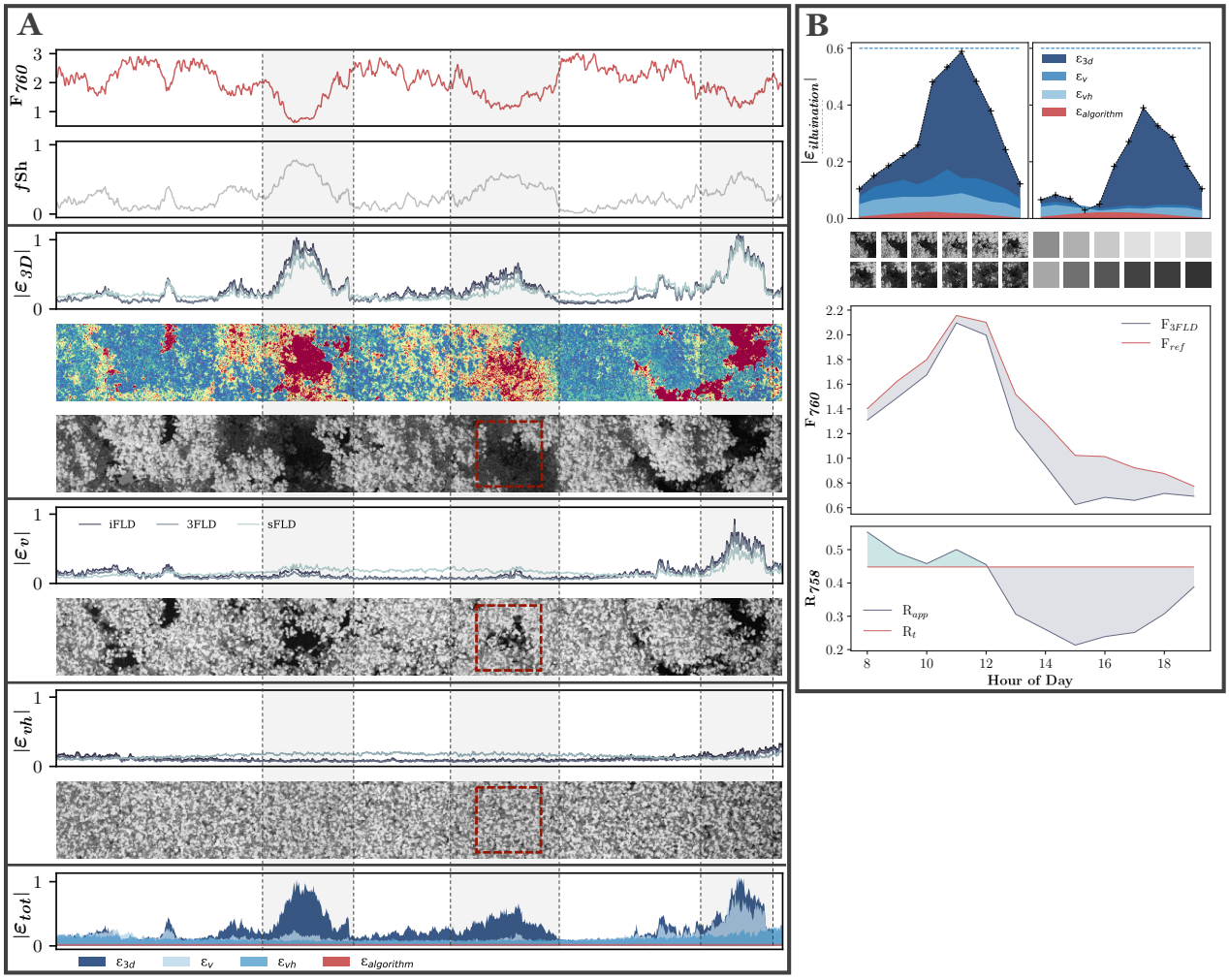

Figure 7: **(A)** 4x40m transect through the 3D forest and its structural abstractions at 2PM (SZA=24°), showcasing: reference fluorescence at 760nm (F_{760}) [mW $m^{-2}nm^{-1}sr^{-1}$], shadow fraction (fSh) [%], and illumination errors ($|\varepsilon|$) [-] for all three mock-ups (3D, v, vh) and each the tested algorithms (sFLD, 3FLD, iFLD). **(B)** Illustration of the upscaling effect on the illumination error, accompanied by the daily cycle of both true and apparent fluorescence (F_{ref}, F_{3FLD}), as well as true and apparent reflectance (r_t, r_{app}).

Summary:

- Algorithm errors were found to be small ($|\varepsilon_{alg}| < 4\%$) and spatially invariant, but showed strong dependency on SZA (exhibit bell-shaped pattern).
- Illumination errors were found to be highly dynamic in space, time and with changing structural complexity ($|\varepsilon_{ill}| \in [0\%, 180\%]$).
- Temporal dynamics of the illumination error is mainly determined by the atmosphere RT that controls the spectral differences between the downwelling sun and sky radiation.
- The spatial dynamics of the illumination error is mainly determined by the structural complexity that controls the local shadow potential.
- On average, 30 % of total $\varepsilon_{illumination}$ could be linked to the vertical forest structure and roughly 20 % to the horizontal heterogeneity.

4.2 Impact of the Vegetation Radiative Transfer on Illumination Error

This section focuses on the spectral alteration of canopy entering light during multiple scattering within the vegetation body and its potential impact on the accuracy of SIF retrievals. To properly disentangle the surface irradiance into its origin constituents the vegetation-RT was conducted separately for direct solar irradiance (E_{sun}) and diffuse sky irradiance (E_{sky}) at various scattering orders (1 vs. 100).
As shown in the previous section, the atmosphere RT creates different absorption band depths for diffuse and direct light emerging their maximum difference around midday. Consequently, the downwelling irradiance measured above the canopy (E_{TOC}) is a specific mixture of both light sources. Fractional changes of E_{sun} (direct) and E_{sky} (diffuse) at the vegetation surface should therefore lead to infilling artifacts.
Interestingly, the direct to total light ratio ($R_{dir/tot}$) could only explain around 30% of the variability of the illumination error in the tested virtual forest scene. Especially in the fully shaded areas, where $R_{dir/tot}$ is zero, a high local error variation was found (see Figure 8B). This result suggests that additional processes than the blocking of direct light by vegetation structures appear to influence the variability of illumination-induced uncertainties on high spatial resolution.

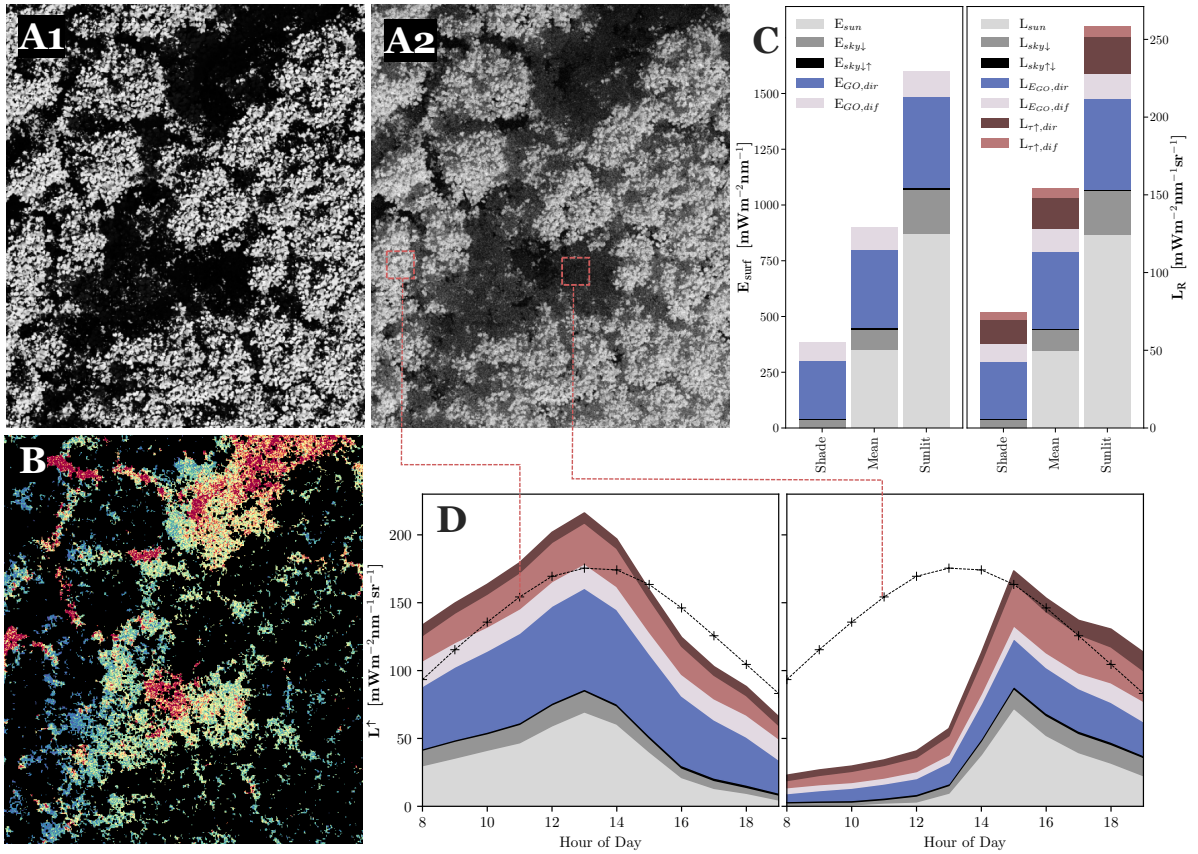

Figure 8: **(A)** Shadow brightening effect between the 1^{st} (A1) and 100^{rd} (A2) canopy scattering in the NIR range ($\lambda : 758nm$). **(B)** Corresponding illumination error map of fully shaded pixels only ($E^{dir} = 0$). Red colors indicate highest ε_{ill}, blue colors indicate lowest ε_{ill}. **(C)** Separation of surface entering and exitinng fluxes, based on their origin. Surface irradiance budget (left) and surface radiance budget without Fs emission (right). **(D)** Temporal variation of canopy leaving nadir radiance (L) at two distinct positions. Black, dashed line denotes to the scene average L. (Please note that A-C correspond to 11AM and A-B is an illustrative subsection of 25x18m.)

Indeed, contributions from geometric-optical scattering (E_{GO}) were found to be a major source of irradiance at the canopy surface layer as seen from nadir ($E_{surf} = E_{sun} + E_{sky} + E_{GO}$) and showed pronounced spatial and diurnal variations (average E_{GO}= 48% at λ=758nm, SZA=31°). Scattering contributions from the surroundings cause an extensional shadow brightening in the NIR range as illustrated in Figure 8A. By contrasting fully shaded and sunlit pixels (Figure 8C) it is noticeable that sunlit pixels receive more E_{GO} in an absolute manner, but the relative proportion of E_{GO} is much higher in shaded pixels, since they do not

receive any sun light and only little sky radiation.
Moreover, E_{GO} can be further divided upon its origin into initially direct or initially diffuse light. Notably, the dominant fraction of canopy scattered irradiance was attributed to initially direct light (E_{GO}^{dir}) (see Figure 8C), with a slightly improving influence of E_{GO}^{diff} at higher SZA (not shown). In fully shaded regions, on average 66% of surface E was found to origin from scattered direct light. By assuming that E_{GO}^{dir} preserve its initial spectral characteristics (lower ABD_{O_2A}) during the multiple scattering it strongly increases the influence of direct light in shaded pixels ($E'_{dir} \approx E_{sun} + E_{GO}^{dir}$).
A similar picture emerges when examining the fractional composition of the upwelling radiance (L_R), which comprises the sensor-reflected surface irradiance, with an additional component arising from the transmitted radiance from deeper understory layers (L_τ) (see Figure 8C). At SZA=31°, L_τ contributes on average 18% of the total $L_\uparrow$ and also originates mainly from initially direct light.
The reported scattering of initially direct light into shaded regions is an important process since it was found to reduce the ABD discrepancies between the surface and the TOC by 58% in shaded regions and 37% across the entire forest scene as depicted in Figure 9C.
Furthermore, the spatial distribution of GO-scattering was found to be non-uniform and profoundly affected by the geometrical arrangement of canopy elements within the observed pixel-column and its adjacent areas (see Figure 9A). As illustrated in Figure 9B both the decrease of ABD discrepancies and the magnitude of the illumination error can be described as a direct function of the magnitude of GO-scattering. A strong exponential relationship emerged between the illumination error (ε_{ill}) and the intensity of GO-scattering in fully shaded regions. Similarly, a correlation of analogous nature was observed between the ABD discrepancies ($\Delta ABD_{|surf-TOC|}$) and GO-scattering in fully shaded regions. Both relationships indicate that the severity of the illumination error diminishes under strong influence of initially direct light.
It seems that the redistribution of first-order inserted light energy in the NIR range appears to mitigate the spectral differences in shadows and potentially lead to a dampening of the severity of the illumination error in shaded regions.

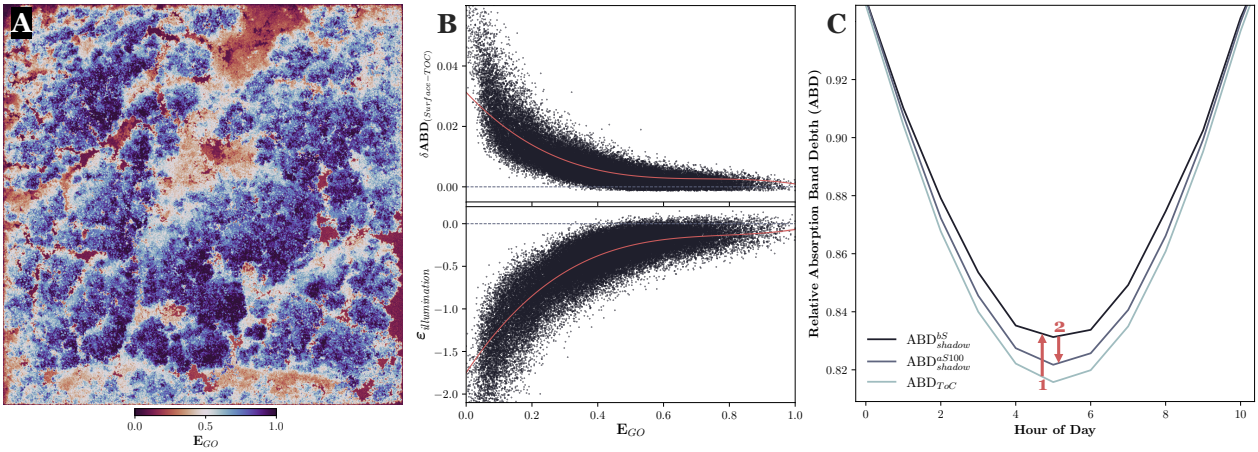

Figure 9: **(A)** Normalized intensity of geometric optical (GO) scattering at 11AM. **(B)** Relationship between the discrepancies in absorption band depth at the surface and ToC ($\delta ABD_{surf-ToC}$), and the normalized intensity of GO-scattering (E_{GO}) in fully shaded pixels (N=247'524pixels) (upper plot). Relationship between the illumination error ε_{ill} and E_{GO} in fully shaded pixels (bottom plot). Please note that ε_{ill} here does not correspond to the absolute error. The negative values represent the strong underestimation of Fs in shaded regions, witch gets better under higher influence of GO-scattering. **(C)** 1. Increase of ABD in fully shaded pixels (relative to ToC) due to blocking of direct light before scatterig (bS). 2. Decrease of ABD discrepancies in the shaded pixels relative to ToC as a result of GO-scattering (after 100^{rd} scatterings).

The presence of direct light in areas that inherently lack direct illumination reduces the sensitivity of the illumination error towards shadows in a classical sense. Consequently, the $R'_{dir/tot}$ ratio (including E_{GO}^{dir} as part of direct light) was able to explain a much higher fraction (62%) of the variability of the illumination error (R^2 : $0.62, p < 0.001$) (see Appendix 2). However, still 38% could not be explained. This is caused by the fact, that the canopy scattered sun and sky light (E_{GO}) do not keep their initial spectral signatures. Mainly two alterations **(Alt1-2)** were identified that potentially lead to non-linearities:

(Alt1:) The contributions from GO-scattering within a canopy element (pixel) was found to be wavelength dependent. In the limited retrieval range centered around the O_2A feature ($\lambda \in [754, 775nm]$), the subtle reduction in the scattering albedo ($dR/d\lambda \neq const.$, $d\tau/d\lambda \neq const.$) of green vegetation towards the red edge resulted in a relative decrease of surface irradiance ($E_{surface}$) and upwelling $L_{\uparrow}$ towards the left reference shoulder. This discrepancy becomes apparent when compared to E measurements taken at the top of the canopy (ToC), as visualized in Figure 10A. The degree of the leftward shift in the spectral signature is driven by E_{GO} and is a direct function of the scattering order - With each successive scattering event, the likelihood of a photon being absorbed increases slightly towards the VIS range.
The relative reduction of E_{surf} at the left reference band ($\lambda = 758nm$) compared to the right reference band ($\lambda = 774nm$) is approximately 5%. Notably, it is more pronounced in shaded pixels (8%) compared to sunlit pixels (3%).
Furthermore, the leftward alteration is particularly higher when looking at the upwelling $L_{R\uparrow}$ (Sunlit: 5%, Sunlit:10%) because of an additional scattering event and the significant influence of the highly altered upward transmitted flux from below ($L_{\uparrow\tau}$).
This is an important finding since the subtle spectral depletion of $L_{R\uparrow}$ was found to play a pivotal role in the tendency of radiance-based algorithms to overestimate the true fluorescence emission (F_{ref}) under fully illuminated conditions. Since the sFLD algorithm solely relies on the left reference band this effect is most pronounced leading to a higher base uncertainty under well illuminated conditions, as already observed in the previous chapter (see Chapter 4.1, Figure 7).
In a broader wavelength context, however, the influence of E_{GO} was found to be drastically reduced towards the VIS range, caused by the increased absorption of green vegetation on the left side of the red edge (not shown, see Appendix 3).

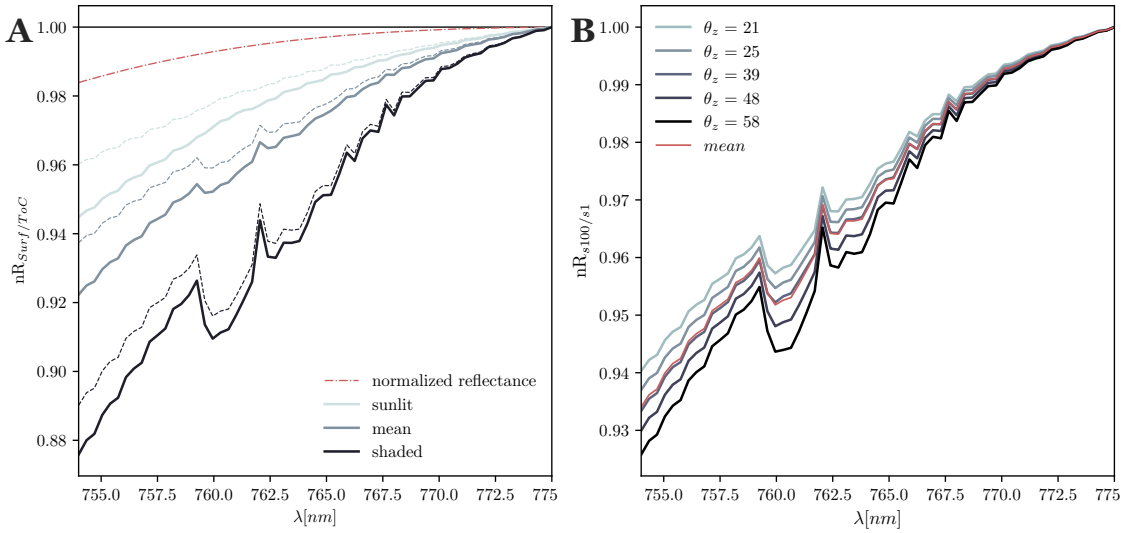

Figure 10: Alterations around the spectral signature of the O_2A absorption feature induced by canopy multiple scattering. **(A)** Surface irradiance E (dashed lines) and upwelling reflected radiance (L_R) (solid lines) normalized using the ToC irradiance (E_{ToC}). $nR_{Surf/ToC}$ was calculated separately for sunlit and shaded pixels. Curves correspond to the illumination conditions at 11AM. **(B)** Normalized Ratio between the nadir reflected radiance (L_R) of the 1^{st} scattering relative to the 100^{th} scattering event for different solar zenith angles θ_s ($nR_{s100/s1}$).

(Alt2:) A second alteration arising from the canopy multiple scattering involves the elongation of individual photon path lengths. This effect is somewhat interlaced with the $\varepsilon_{atmosphere}$ (see Chapter 2.2.2) since not only the path from sensor to the surface and vice verca contribute to increased oxygen absorption, but also the path elongation from canopy scattering itself. The subtle deepening in the O_2A feature related to GO-scattering, can partially offsetting the previously described dampening effect and varies with the Solar Zenith Angle (SZA) throughout the day. As illustrated in Figure 10B, the minimal average deepening occurs around midday (0.45%), whereas the peak average deepening (0.95%) occurs during high SZA periods in the morning and evening when the sun's rays penetrate more deeply into the forest.

Summary:
E_{GO} is a significant contributor to surface irradiance and has a notable impact on the magnitude of ε_{ill}.

- *GO-scattering:* The pronounced scattering of initially direct light into shaded areas diminishes the ABD discrepancies between the surface and the ToC by up to 58%. This process potentially mitigates the severity of the illumination error.
- *Alterations in Spectral Signatures:* Wavelength-dependent scattering-intensities within the canopy shift the spectral signature towards the red edge. This alteration is a primary factor for the systematic overestimation observed in FLD algorithms, particularly sFLD, under fully illumination conditions. The leftward shift in the spectral signature around the O_2A feature is a direct function of the leaf optical properties and the scattering order.
- *Photon Path Length Elongation:* Multiple scattering elongates photon paths, which in turn affects oxygen absorption and deepens the O_2A feature. This deepening ranges between 0.45% and 0.97%, leading to an amplification of ε_{ill}, especially during high Solar Zenith Angles.

4.3 Scale Dependency of Illumination Error

So far, this study has focused on high-resolution SIF retrievals (4cm x 4cm), where individual pixels represent either sunlit or shaded leaves. In this section, we explore the effects of upscaling the retrieval resolution from the leaf level to the canopy- and ecosystem level, thereby gradually mixing different illumination conditions together.

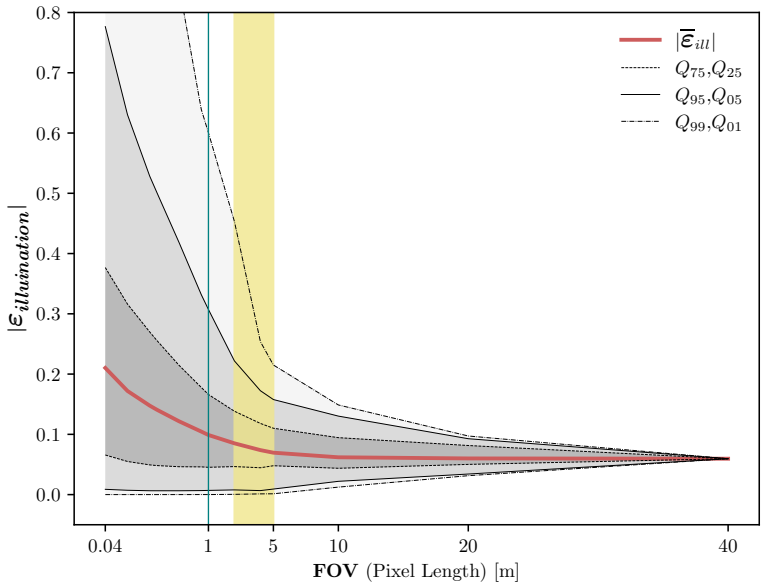

Figure 11: Scale Dependency of the Illumination Error: This Figure illustrates the scale dependency of the illumination error across various remote sensing footprint sizes, using the iFLD algorithm as an example. The yellow rectangle denotes the typical Field of View (FOV) range for tower-based SIF retrieval setups. Note: The x-axis scale below 1m is expanded to accommodate the pronounced exponential increase in $\varepsilon_{illumination}$.

As illustrated in Figure 9A, the illumination error exhibits a strong scale-dependency when considered from two aspects.

(i) Firstly, the average illumination error within the whole forest section (red line) decreases with an increased retrieval footprint and stabilizes at a constant value. This observed convergence onto a "base-uncertainty" is associated with the average shadow content in the forest scene (at a given time) and remains constant once reached regardless of a further increase in the FOV. In the case of the iFLD algorithm (represented in Figure 11), the average scene uncertainty exponentially decreases from 21% at leaf resolution to a fully stabilized value of 8% at a FOV of roughly 20m.

(ii) A second and much more important effect was observed regarding the internal variability around the average illumination error, which also exponentially reduces with larger measurement footprints (represented by the gray area). This is caused by higher spatial heterogeneity at small observation scales. For example, a randomly selected small pixel may lie in a deep vertically structured shadow gap, receiving no direct light at all, or is located at an exposed tree crown which is fully illuminated or at any intermediate condition between. On the other hand, increasing the field of view dilutes potential shadow extremes and underlying RT, resulting in a significant reduction in the inter-pixel variability around the average error.This implies that larger FOV's lead to a more representative and stable fluorescence estimation although the average shadow error might be the same. In the case of the iFLD (see Figure 11), the strong fluctuations around the mean >100% occuring at the leaf level and were strongly reduced to less than 5% by simply increasing the FOV to 20m pixel size.

To sum up, Figure 11 provides a comprehensive overview of the influence of illumination artifacts on passive remote sensing observations of fluorescence. It underscores that insufficient knowledge about the incident E field within a pixel can lead to substantial uncertainties, as the pixel size become small. Vice versa, illumination artefacts can be substantially reduced by simply increasing the sensor footprint. The base uncertainty, however, can not be further reduced without correction.
In the tested virtual forest section, a pixel area smaller than $1m^2$ (green line) — a size typically achieved in airborne or UAV missions over intricate forest vegetation — is particularly susceptible to illumination artifacts. Without shadow field correction or enhanced irradiance input, significant errors arise.
The yellow rectangle representing the typical observation scale of a tower-based SIF retrieval-setup using a conical non-imaging Spectroradiometer (FOV: 4-25m2). Such retrievals fall within a critical transitional zone, bridging the gap between a sharp non-linear rise in error and the converged base level uncertainty.

To close the result section, Figure 9B summarizes the retrieval uncertainties arising from the lack of knowledge about the incident irradiance field for all tested algorithms on three different spatial scales: the leaf-level (16cm2), the canopy level (9m2), and the ecosystem level (900m2).
Overall, the three algorithms (sFLD, 3FLD, iFLD) were found to perform similarly when treated with inaccurate irradiance input. However, there are noticeable scale-dependent differences. The sFLD method exhibits the least error variability at high spatial resolutions but produces the highest base uncertainty as scales increase (at the canopy and ecosystem levels). In contrast, the 3FLD and iFLD methods display greater error variability at high spatial resolutions but yield the most accurate F retrievals at lower resolutions. Excluding extreme cases (Q99), the 3FLD method demonstrates the most consistent results throughout the upscaling process.

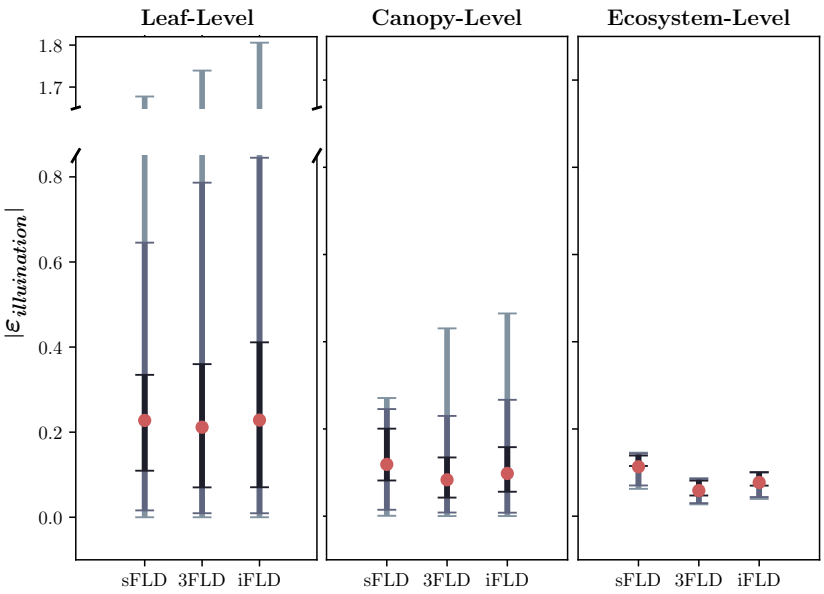

Figure 12: Error sensitivity of all tested algorithms along three retrievel scales: Leaf-level (16cm2), Canopy level (9m2), Ecosystem level (900m2).

Summary:

- The average illumination error decreases with an increased retrieval footprint, stabilizing at a base level uncertainty.
- The variability around the average illumination error reduces exponentially with larger measurement footprints.
- By expanding the Field of View (FOV) from individual leaves to the broader ecosystem scale, retrieval uncertainties, which initially varied from 0% to 180%, are substantially narrowed down to a consistent range of 4-9%.

5 Discussion

5.1 Algorithm Error:

Algorithm errors were found to be structurally and spatially consistent, i.e., remaining unaffected by varying illumination conditions or changing structural complexities and therefore, showed no sensitivity to retrieval footprint size. However, they varied with the Solar Zenith Angle (SZA), peaking around midday. If the actual E field was perfectly known, all tested algorithms achieved low retrieval uncertainties (sFLD $< 4\%$, 3FLD $< 2.5\%$, iFLD $< 0.4\%$).
The difference between sFLD and the more advanced iFLD algorithm is significant (factor of ten), suggesting that non-linear modeling of r and F can greatly reduce algorithm methodological uncertainties.
These findings emphasize the capability of radiance-based algorithms to accurately retrieve fluorescence emissions when provided with accurate irradiance input. Simultaneously, it highlights the limited potential for enhancements in FLD-based methods and the need to rather focus on improving the irradiance input when dealing with high spatial resulted data.

5.2 Illumination Error:

Illumination errors, arising from the lack of knowledge about the actual surface E field, on the other hand, were found to be highly variable in their spatial, structural, and temporal characteristics.
A comprehensive analysis of the coupled atmosphere-vegetation RT concludes that the illumination uncertainties are mainly sensitive to:

(i) the sun zenith angle,
(ii) the structural complexity of the vegetation surface,
(iii) the intensity of geometric-optical scattering and
(iv) the observation footprint (i.e., sensor FOV)

The first two points determine the error potential (Chapter 5.2.1), while the latter two control the actual severity of an illumination artifact in a retrieved pixel (Chapter 5.2.2 and Chapter 5.2.3).

5.2.1 Error Potantial

The DART simulations provided evidence that the likelihood of producing significant illumination artifacts varies over time. Fully shaded pixels at low SZA demonstrated notably greater illumination errors, up to threefold, compared to those at high SZA (see Appendix 2). Consequently, throughout the entire scene, the diurnal variations of the illumination error generally follow a bell-shaped pattern, with a plateau-shaped peak at midday, and reduced effect sizes (≈-50%) in the morning and evening. However, this pattern can be significantly influenced by local illumination conditions.

The role of atmosphere RT: The temporal dynamics of the illumination error can be explained by the atmosphere RT, with the Solar Zenith Angle (SZA) being the primary factor determining the individual path lengths for direct and diffuse light, which in turn affects the spectral shape and intensity of both E components [11].
At midday, the spectral differences between direct sunlight (Esun) and diffuse sky light (Esky) were found at their peak, resulting in the highest potential for infilling artifacts (ΔABD$_{|dif-dir|}$=max).
At the same time, the intensity of direct light relative to diffuse light was also at its maximum. Consequently, the steepest ABD gradients between the surface (E$_{surface}$) and the top of the canopy (E$_{ToC}$) can be achieved when direct light is fully obstructed by the vegetation surface at midday (ΔABD$_{|surf-ToC|}$=max).
However, it is important to note that all DART simulations in this study used a static atmospheric model under clear sky conditions. In real-world scenarios, the atmosphere is way more dynamic, and the solar zenith angle (SZA) not the only control of the photon path length. Studies by Guanter et al. [22] and more recently Sabater et al. [55] highlight that diurnal variations in atmospheric path length can also be influenced by factors such as fluctuating aerosol concentrations, changing cloud cover, and diurnal variations in pressure and potential temperature profiles, making the illumination error potential more variable and less affected by SZA in real world time-series.
Especially the effect of clouds on the accuracy of fluorescence retrievals would be an interesting topic for further investigation. It is conceivable, that cloudy weather or cloud shadows may have a reducing effect on illumination artifacts as thought from two perspectives. Firstly, the higher intensity of diffuse radiation minimizes overall shading effects within the canopy because the illumination comes from a larger portion of

the sky hemisphere, making it more isotropic [54]. Secondly, due to the blocking of direct light by clouds instead of vegetation surfaces, the ABD discrepancies between the surface and ToC should be remarkably reduced. In other words, clouds will mute the directional component of light and therefore mute the impact of the atmosphere RT on the formation of illumination artifacts, leaving the canopy RT as the only source of error.

The role of surface texture: The second driver that could enhance the potential for illumination error is the surface texture, which determines the overall shadow fraction (fSh) present in a scene at a given SZA. The DART simulations highlighted a marked decrease in the amount of fully shaded pixels as the 3D forest scene underwent higher levels of homogenization (SF_{3d}:30%, SF_v:25%, SF_{vh}: 18%).
This variation can be explained by different types of shadows that emerge at different levels of surface complexity. The fully homogenized forest abstraction only contains the fine-scaled, homogeneously distributed self- and cast-shadow at the leaf level, which is mainly influenced by volumetric scattering. By adding horizontal variability, shadow gaps build up as an additional source of shadow and the dominance of geometric-optical scattering increases. These gaps are mainly produced from non-random tree spacing and horizontal leaf clumping [13]. Finally, by adding the vertical structure to a realistic 3D forest model, cast shadows from exposed canopy elements and branches additionally occur, which can cover larger areas within a forest.
The link between the vegetation structure and shadow potatial has been reported in previous studies. Lopatin et al. [38] compared the proportion of shaded crowns during the course of the day. They confirmed that canopies of certain species are shaded more prominent and during a large portion of the day, whereas canopies from other species are mostly sunlit. As a consequence, different forests produce longer and shorter optimal acquisition periods for RS measurements .
Also, Kane et al. [28] and Hilker et al. [25] found that Canopy self-shadowing strongly correlates with the canopy's geometric complexity.

To sum up, it can be stated that mainly three mechanisms control the illumination error potential: (i) The spectral difference between the downwelling sun and sky light around the O_2A absorption band, (ii) the proportion of direct to diffuse downwelling irradiance, and (iii) the structural complexity of the vegetation surface (i.e., shadow potential). The error potential is greatest when a surface, which casts significant shadows even at low SZA, is illuminated by sun and sky light exhibiting their maximum spectral differences. These findings provide valuable insight into complex temporal and spatial interactions between atmosphere and surface and show that a minimal shadow cast does not automatically provide the best conditions for achieving low illumination uncertainties.

5.2.2 The Role of Canopy RT

While the overall error potential was found to be strongly controlled by the atmosphere RT in combination with the surface texture, the actual severity of the illumination error at a given pixel is primarily driven by the canopy RT. This study identified three primary mechanisms that have a profound impact on the accuracy of SIF retrievals using the O_2A band:

(i) The scattering of initially direct light into shaded regions (Dampening effect).
(ii) The depletion of the left reference shoulder with increasing scattering order (O_2A shape alteration).
(iii) The subsequent alteration of oxygen absorption depths (O_2A depth alteration).

Error dampening effect: The simulation output provide evidence that the surface irradiance field ($E_{surface}$) at a specific canopy element is merely a straightforward linear combination of the entering sun and sky light (E_{dir}, E_{dif}). Instead, it is significantly influenced by the dominance of GO-scattering from the surroundings, which introduces an additional source of irradiance (EGO) at the canopy surface layer. While the contributions from multiple scattering were minimal in the VIS range (<10% of E_{surf}), they played a significant role in shaping the incident E field within the NIR range ($\approx$ 48%), a finding also observed in previous studies (e.g., [66]).
The high proportion of initially direct light present in E_{GO} is relevant for the accuracy of O_2A retrievals. This is particularly noticeable in shaded regions, where it leads to an indirect presence of the spectral characteristics of direct light (i.e., reduced ABD) even though these areas are completely obstructed from sunlight. Therefore, the scattering of initially direct light into shaded regions has a cascading effect on the O_2A absorption band depth discrepancies between the surface and ToC ($\Delta ABD_{|surf-ToC|}$). A substantial decrease in these discrepancies was observed - 58% in shaded areas and 37% over the entire forest scene, leading to a dampening effect of the severity of the illumination error, particularly in shaded areas.
Several conclusions can be made from this finding. The pronounced redistribution of first order inserted light energy during canopy multiple scattering strongly dilutes the error contrast between sunlit and shaded

vegetation, making illumination artifacts within O_2A retrievals less sensitive to shadows in a classical sense. Conversely, the strongly reduced influence of multiple scattering detected on the left side of the red edge (see Appendix 3) will lead to an absence of this dampening effect. As a result, fluorescence retrievals using the O_2B band are expected to exhibit higher error contrasts between sunlit and shaded regions and therefore are more sensitive to illumination artifacts. More research would be needed to investigate the impact of canopy RT in the VIS range on illumination effects of O_2B retrievals. Moreover, the strong wavelength dependency of E_{GO} will also effect reflectance based indices, especially when bands between the VIS and NIR would be used.
However, to come back into line, the relationship between the intensity of GO scattering and the illumination error was found to be non-linear. This suggests that there are other factors at play, in addition to the dampening effect. Indeed, E_{GO} was found to undergo several alterations during the multiple scattering process in the canopy.

Alteration of the O_2A absorption depth: The DART simulations revealed a significant decrease in the spectral signature of $E_{surface}$ and L_{ToC} relative to E_{ToC} towards the left reference shoulder of the O_2A feature. This alteration is closely related to the optical properties of the leaves and the scattering order of exiting radiance.
Despite the near-constant reflection of green vegetation in the vicinity of the O_2A feature, there's a subtle increase in absorption towards the red edge (leftwards). This increase in absorption affects the scattering albedo, making it less likely for photons in the left shoulder to scatter. As a result, there's a noticeable drop in the spectral signature, which becomes more evident with each subsequent scattering event.
Sunlit pixels generally showed the smallest relative changes ($\approx$5%), while shaded pixels exhibited more significant alterations of $\approx$10%. This can be explained by the fact that shadows are more likely to appear in local depressions where the number of scatterings needed for a photon to escape the canopy is higher compared to the exposed canopy surfaces.
However, this is an important finding, because the leftward drop in the spectral signature of L relative to E_{ToC} was found to be the main reason for the overestimation of radiance-based retrieval algorithms (i.e., sFLD, 3FLD) under fully illuminated conditions. Especially for the sFLD algorithm, which only uses a left reference band, the overestimation of SIF can be significantly amplified under presence of strong GO-scattering.
Cendrero-Mateo et al. [7], among others, have reported the systematic overestimation of FLD based algorithms during high fluorescence emission and related this behavior to the non linear relationship of r and F within the O_2A retrieval range. This study reinforces this interpretation and offers deeper insights into how multiple scattering can intensify these uncertainties with each subsequent scattering event.
Moreover, the slope of this depletion is expected to show a strong correlation with the intensity of canopy multiple scattering. As such, it could potentially act as a proxy for the degree of geometric-optical scattering within or between vegetation structures. However, further research is required to delve into this topic.

Scattering induced deepening of the O_2A feature: A second prominent alteration, is related to the oxygen transmittance effect described as a part of the atmosphere error in chapter 2.2.2. The DART simulations showed that not only the path from a sensor to the surface and back to the sensor can introduce additional deepening of the O2A bands ($\varepsilon^{sFLD}_{atmosphere}$), but also the photon path elongation solely induced by the canopy multiple scattering.
The deepening, related to the canopy scattering was found to be in the range between 0.45-0.95%. While, the effect of molecular oxygen absorption seems to be large for such short distances, it is essential to recognize that ABD deepening is not only a function of photon path length. Building on the findings of Sabater et al. [56], oxygen absorption is also proportional to air pressure. Thus, even a few meter distance between the target and the sensor at the Earth's surface, where the air pressure is at its maximum, can lead to significant deepening in the absorption band [56, 35].
At high SZA, when the incoming rays penetrate the canopy at a flatter angle, the additional O_2A deepening was found to be highest. This indicates stronger multiple scattering in the morning and evening, which is consistent with the findings of previous studies [66].
Upon closer examination, the DART simulations provided evidence of an additional O_2A deepening associated with canopy multiple scattering. These effects are significant and should be adequately accounted for in correction methods. Furthermore, it is crucial to highlight that this additional O_2A deepening primarily arises from the spectral alteration of E_{GO} during canopy multiple scattering in combination with the altered upward transmitted flux from deeper canopy layers (L_τ). Given that the influence of multiple scattering strongly diminishes in the O_2B window (VIS domain), it can be expected that this additional deepening predominantly affects O2A retrievals.

5.2.3 Scale dependency:

Of all investigated effects, the sensor footprint has the most important influence on the effect size of illumination errors.
Within the virtual forest scene, both the average illumination error and the variability around the mean error decreased exponentially and converged to a stable base level of uncertainty. Quantitatively, at finer leaf scale, the illumination artifacts exhibited substantial fluctuations, ranging from almost negligible ($\approx 0\%$) to a substantial 180%. By the time observations were scaled to the ecosystem level, the variability converged and stabilized consistently, falling within a narrow 4-9% range.
The scale dependency of remote sensing observations is a well reported issue [71] and also affects florescence retrievals [51]. In terms of the illumination error it can be explained by the fact that small scale information cannot be used as a substitute for regional scale information [71, 48], since different processes appear to be dominant at different scales. At high spatial resolution the apparent irradiance field is extremely complex and illumination artifacts are mainly driven by the canopy 3D structure in combination with isotropic, volumetric and geometric-optical scattering. As the footprint scales up to the ecosystem level, the intricate local error variations stemming from the high shadow dynamics, and multifaceted RT processes become averaged and manifest in a base level uncertainty that encapsulates these complexities.
Several implications can be made from this finding.
First of all it can be stated that the lack of knowledge about the incident irradiance field is primarily a problem of fluorescence retrievals using a high spatial resolution. In this study the critical footprint below which, artefacts became unacceptably large was found to be 1m. At such retrieval scales the assumption of a fully illuminated and uniformly flat Earth surface does not longer hold and the treatment of E as a discrete property without differentiate between direct and diffuse components becomes a substantial source of uncertainty. To date, there are already some approaches published trying to minimize the impact of varying illumination effects (e.g., [14, 41]). However more research is needed to push the efficiency of correction methods forward.
Moreover, it can be concluded, that tower-based retrieval set-ups are in a critical zone. The quality of the timeseries in term of retrieval accuracy can be substantially improved by an increase of the footprint. This can also be of interest to better link the fluorescence retrievals to eddy-covariance GPP fluxes rather than tracking the local variation of PAR induced by varying shadow fields in a too small FOV. However, increasing the sensor altitude is not a good solution because this would increase the atmosphere error (see Chapter 2.2.2). Liu et al. [37] tried to improve the footprint by replacing conical set-ups with hemispherical observations under cosine-corrected foreoptic. With this method they achieved a much larger field of view and were able to better match the footprint of the GPP flux measurements.

5.2.4 Limitations

When considering the results of the radiative transfer (RT) analysis presented in this study, including the magnitudes of illumination artifacts, it is important to note that they stem from a single mock-up representing an intermediate-sized virtual forest section (40x40m).
In reality, forest ecosystems exhibit vast diversity in aspects such as species, canopy shapes, background properties, terrain, leaf angle distributions, biochemistry, or environmental conditions. This diversity inevitably influences the underlying radiative transfer. In this study several simplifications were made that need critical evaluation.
Modelling limitations: Due to computational limitations, the canopy radiative transfer was modeled with 100 discrete scattering directions in the whole 4π space, without oversampling the hot-spot up- and downward directions. An accurate simulation would require much finer scattering angles during canopy RT.
Monte Carlo Noise poses another challenge that can introduce uncertainty. This noise, combined with scene variability, are common sources of uncertainty in DART-Lux output and can be reduced by increasing the ray density per direction per pixel [17]. Within this study a high sample density per pixel of at least 180 was applied, but it may not completely eliminate uncertainties, especially in very dark pixels.
Moreover, all vegetation surfaces within the forest scene were treated as Lambertian surfaces, neglecting leaf specular reflection. In reality, the scattering phase function of green leaves typically falls between 'Lambertian' and 'specular,' often with peaks in the specular and hot-spot directions [17]. Neglecting the directional scattering behavior not only distorts the RT in terms of surface reflactence anisotropy but can significantly impact the overall accuracy of the canopy RT, particularly the first-order scattering.
Furthermore, the focus on nadir orthoimages is a simplification. Many retrievals typically have a view zenith angle around 20° with a conical field of view. Inclined observations increase the influence of sun azimuth angles, leading to hotspot effects when the sun is behind the sensor and more pronounced shadow fields when

the sun is behind the scene. The impact of inclined sensor view on the severity of the illumination error requires further investigation.
Structural limitations: The 40x40m virtual forest scene offered diverse structural variations, ideal for examining spatial and temporal effects of the illumination error. However, its structural limitations should be considered when assessing the results.
To achieve comparability with the two structurally abstracted mock-ups, all stems and branches of the trees were excluded from the scene, and the ground was modelled as a flat surface fully covered with vegetation, which differs from the complexity of real-world forest environments.
Furthermore, the average LAI of 8.2 is notably higher than for typical mid-latitude deciduous forests [29]. Also, the Leaf Angle Distribution (LAD), as modeled by the authors of the original mock-up [6], do not follow a clear distribution (e.g., planophile, erectophile, etc., see [21]). LAI and LAD are important structural parameters that can impact the illumination field, the distribution of shadows, and the diffusion depth of light into the canopy. Therefore, further simulations under controlled variations of LAI and different LAD are recommended to explore their impacts on the illumination error.
Moreover, the reduction of LAI will increase the importance of woody components and forest floor in the canopy RT and hence, introduce additional complexities (e.g., mixing of spectral signatures [4]).
Leaf biochemical limitations: The study assumes that all canopy components have identical biochemical compositions, leading to uniform leaf optical properties and fluorescence yields. Fluctuations in leaf optical properties under real-world conditions can further impact the multiple scattering mechanisms during vegetation RT.

However, it can be expected that these limitations do not substantially impact the primary conclusions drawn about the illumination error.

6 Conclusion:

This study provided valuable insights in the spatial and temporal behavior of illumination artifacts. It highlights that both the atmosphere RT as well as the canopy RT were substantially involved in the formation process of illumination uncertainties.
The sun zenith angle was identified as the major control that shapes the ABD differences between the downwelling sun and sky light and favours the occurrence of larger artifacts around midday.
Within the canopy, strong multiple scattering processes were detected in the NIR domain. The scattering of initially direct light into shaded regions was identified as an important process that diminishes the ABD discrepances between the surface and the ToC and hence, lead to a dampening effect of the illumination error in the O_2A band. However further research would be needed to investigate the role of this effect in the O_2B band which is less influenced by canopy multiple scattering.
Significant alterations in E_{GO}, such as the reduction of the spectral signature toward the left reference shoulder or the further deepening of the oxygen band, could potentially lead to non-linearities in SIF retrievals.
Moreover, the strong scale dependency of the illumination error revealed that the lack of knowledge about the incident E field becomes a substantial problem when footprints drop below a critical size (in this study 1m). The findings emphasize the importance to improve the irradiance input for retrieval algorithms and the need of developing correction methods to overcome the scale issue of fluorescence retrievals. In conclusion, this research has provided a deeper understanding of illumination artifacts and their complexities. As the field of high-resolution fluorescence retrievals continues to evolve, the insights from this study may help to better understand the fine scaled processes that drive illumination uncertainties. There is still much to explore and learn, and this work lays a foundation for future research aimed at improving remote sensing accuracy.

References

[1] S. K. Alavipanah, M. Karimi Firozjaei, A. Sedighi, S. Fathololoumi, S. Zare Naghadehi, S. Saleh, M. Naghdizadegan, Z. Gomeh, J. J. Arsanjani, M. Makki, et al. The shadow effect on surface biophysical variables derived from remote sensing: A review. *Land*, 11(11):2025, 2022.

[2] L. Alonso, L. Gomez-Chova, J. Vila-Frances, J. Amoros-Lopez, L. Guanter, J. Calpe, and J. Moreno. Improved fraunhofer line discrimination method for vegetation fluorescence quantification. *IEEE Geoscience and Remote Sensing Letters*, 5(4):620–624, 2008.

[3] S. Bandopadhyay, A. Rastogi, and R. Juszczak. Review of top-of-canopy sun-induced fluorescence (sif) studies from ground, uav, airborne to spaceborne observations. *Sensors*, 20(4):1144, 2020.

[4] C. C. Borel and S. A. Gerstl. Nonlinear spectral mixing models for vegetative and soil surfaces. *Remote sensing of environment*, 47(3):403–416, 1994.

[5] N. Butt, G. Campbell, Y. Malhi, M. Morecroft, K. Fenn, and M. Thomas. Initial results from establishment of a long-term broadleaf monitoring plot at wytham woods, oxford, uk. *University Oxford, Oxford, UK, Rep*, 2009.

[6] K. Calders, N. Origo, A. Burt, M. Disney, J. Nightingale, P. Raumonen, M. Åkerblom, Y. Malhi, and P. Lewis. Realistic forest stand reconstruction from terrestrial lidar for radiative transfer modelling. *Remote Sensing*, 10(6):933, 2018.

[7] M. P. Cendrero-Mateo, S. Wieneke, A. Damm, L. Alonso, F. Pinto, J. Moreno, L. Guanter, M. Celesti, M. Rossini, N. Sabater, et al. Sun-induced chlorophyll fluorescence iii: Benchmarking retrieval methods and sensor characteristics for proximal sensing. *Remote sensing*, 11(8):962, 2019.

[8] J. Chen and S. Leblanc. Multiple-scattering scheme useful for geometric optical modeling. geoscience and remote sensing. *IEEE Transactions on*, 39(5):1061–1071, 2001.

[9] A. Damm, J. Elbers, A. Erler, B. Gioli, K. Hamdi, R. Hutjes, M. Kosvancova, M. Meroni, F. Miglietta, A. Moersch, et al. Remote sensing of sun-induced fluorescence to improve modeling of diurnal courses of gross primary production (gpp). *Global Change Biology*, 16(1):171–186, 2010.

[10] A. Damm, A. Erler, W. Hillen, M. Meroni, M. E. Schaepman, W. Verhoef, and U. Rascher. Modeling the impact of spectral sensor configurations on the fld retrieval accuracy of sun-induced chlorophyll fluorescence. *Remote Sensing of Environment*, 115(8):1882–1892, 2011.

[11] A. Damm, L. Guanter, W. Verhoef, D. Schläpfer, S. Garbari, and M. E. Schaepman. Impact of varying irradiance on vegetation indices and chlorophyll fluorescence derived from spectroscopy data. *Remote Sensing of Environment*, 156:202–215, 2015.

[12] F. Daumard, Y. Goulas, A. Ounis, R. Pedros, and I. Moya. Measurement and correction of atmospheric effects at different altitudes for remote sensing of sun-induced fluorescence in oxygen absorption bands. *IEEE Transactions on Geoscience and Remote Sensing*, 53(9):5180–5196, 2015.

[13] V. Demarez, S. Duthoit, F. Baret, M. Weiss, and G. Dedieu. Estimation of leaf area and clumping indexes of crops with hemispherical photographs. *Agricultural and Forest Meteorology*, 148(4):644–655, 2008.

[14] D. Fawcett, W. Verhoef, D. Schläpfer, F. D. Schneider, M. E. Schaepman, and A. Damm. Advancing retrievals of surface reflectance and vegetation indices over forest ecosystems by combining imaging spectroscopy, digital object models, and 3d canopy modelling. *Remote sensing of environment*, 204:583–595, 2018.

[15] A. Fournier, Y. Goulas, F. Daumard, A. Ounis, S. Champagne, and I. Moya. Effects of vegetation directional reflectance on sun-induced fluorescence retrieval in the oxygen absorption bands. In *Proceedings of the 5th International Workshop on Remote Sensing of Vegetation Fluorescence, Paris, France*, volume 2224, 2014.

[16] P. Fu, K. Meacham-Hensold, M. H. Siebers, and C. J. Bernacchi. The inverse relationship between solar-induced fluorescence yield and photosynthetic capacity: benefits for field phenotyping. *Journal of Experimental Botany*, 72(4):1295–1306, 2021.

[17] J. P. Gastellu-Etchegorry. *DART USER'S MANUAL (5.10.0)*, September 2023. Accessed: September 29, 2023.

[18] J.-P. Gastellu-Etchegorry, N. Lauret, T. Yin, L. Landier, A. Kallel, Z. Malenovskỳ, A. Al Bitar, J. Aval, S. Benhmida, J. Qi, et al. Dart: recent advances in remote sensing data modeling with atmosphere, polarization, and chlorophyll fluorescence. *IEEE Journal of Selected Topics in Applied Earth Observations and Remote Sensing*, 10(6):2640–2649, 2017.

[19] J.-P. Gastellu-Etchegorry, T. Yin, N. Lauret, T. Cajgfinger, T. Gregoire, E. Grau, J.-B. Feret, M. Lopes, J. Guilleux, G. Dedieu, et al. Discrete anisotropic radiative transfer (dart 5) for modeling airborne and satellite spectroradiometer and lidar acquisitions of natural and urban landscapes. *Remote Sensing*, 7(2):1667–1701, 2015.

[20] T. J. Givnish. Adaptation to sun and shade: a whole-plant perspective. *Functional Plant Biology*, 15(2):63–92, 1988.

[21] N. S. Goel. Models of vegetation canopy reflectance and their use in estimation of biophysical parameters from reflectance data. *Remote sensing reviews*, 4(1):1–212, 1988.

[22] L. Guanter, L. Alonso, L. Gómez-Chova, M. Meroni, R. Preusker, J. Fischer, and J. Moreno. Developments for vegetation fluorescence retrieval from spaceborne high-resolution spectrometry in the o2-a and o2-b absorption bands. *Journal of Geophysical Research: Atmospheres*, 115(D19), 2010.

[23] L. Guanter, Y. Zhang, M. Jung, J. Joiner, M. Voigt, J. A. Berry, C. Frankenberg, A. R. Huete, P. Zarco-Tejada, J.-E. Lee, et al. Global and time-resolved monitoring of crop photosynthesis with chlorophyll fluorescence. *Proceedings of the National Academy of Sciences*, 111(14):E1327–E1333, 2014.

[24] R. Hernández-Clemente, P. R. North, A. Hornero, and P. J. Zarco-Tejada. Assessing the effects of forest health on sun-induced chlorophyll fluorescence using the fluorflight 3-d radiative transfer model to account for forest structure. *Remote Sensing of Environment*, 193:165–179, 2017.

[25] T. Hilker, N. C. Coops, C. R. Schwalm, R. P. S. Jassal, T. A. Black, and P. Krishnan. Effects of mutual shading of tree crowns on prediction of photosynthetic light-use efficiency in a coastal douglas-fir forest. *Tree physiology*, 28(6):825–834, 2008.

[26] J. T. Kajiya. The rendering equation. In *Proceedings of the 13th annual conference on Computer graphics and interactive techniques*, pages 143–150, 1986.

[27] A. Kallel. Flulcvrt: Reflectance and fluorescence of leaf and canopy modeling based on monte carlo vector radiative transfer simulation. *Journal of Quantitative Spectroscopy and Radiative Transfer*, 253:107183, 2020.

[28] V. R. Kane, A. R. Gillespie, R. McGaughey, J. A. Lutz, K. Ceder, and J. F. Franklin. Interpretation and topographic compensation of conifer canopy self-shadowing. *Remote sensing of Environment*, 112(10):3820–3832, 2008.

[29] R. N. Khairiah, Y. Setiawan, L. B. Prasetyo, and P. A. Permatasari. Leaf area index (lai) in different type of agroforestry systems based on hemispherical photographs in cidanau watershed. In *IOP Conference Series: Earth and Environmental Science*, volume 54, page 012050. IOP Publishing, 2017.

[30] D. Kükenbrink, A. Hueni, F. D. Schneider, A. Damm, J.-P. Gastellu-Etchegorry, M. E. Schaepman, and F. Morsdorf. Mapping the irradiance field of a single tree: Quantifying vegetation-induced adjacency effects. *IEEE Transactions on Geoscience and Remote Sensing*, 57(7):4994–5011, 2019.

[31] M. Kvicera, F. P. Fontán, J. Israel, and P. Pechac. A new model for scattering from tree canopies based on physical optics and multiple scattering theory. *IEEE Transactions on Antennas and Propagation*, 65(4):1925–1933, 2017.

[32] P. Latimer, T. Bannister, and E. Rabinowitch. Quantum yields of fluorescence of plant pigments. *Science*, 124(3222):585–586, 1956.

[33] L. Liu, X. Liu, and J. Hu. Effects of spectral resolution and snr on the vegetation solar-induced fluorescence retrieval using fld-based methods at canopy level. *European Journal of Remote Sensing*, 48(1):743–762, 2015.

[34] W. Liu, J. Atherton, M. Mõttus, J.-P. Gastellu-Etchegorry, Z. Malenovskỳ, P. Raumonen, M. Åkerblom, R. Mäkipää, and A. Porcar-Castell. Simulating solar-induced chlorophyll fluorescence in a boreal forest stand reconstructed from terrestrial laser scanning measurements. *Remote Sensing of Environment*, 232:111274, 2019.

[35] X. Liu, J. Guo, J. Hu, and L. Liu. Atmospheric correction for tower-based solar-induced chlorophyll fluorescence observations at o2-a band. *Remote Sensing*, 11(3):355, 2019.

[36] X. Liu and L. Liu. Influence of the canopy brdf characteristics and illumination conditions on the retrieval of solar-induced chlorophyll fluorescence. *International Journal of Remote Sensing*, 39(6):1782–1799, 2018.

[37] X. Liu, L. Liu, J. Hu, and S. Du. Modeling the footprint and equivalent radiance transfer path length for tower-based hemispherical observations of chlorophyll fluorescence. *Sensors*, 17(5):1131, 2017.

[38] J. Lopatin, K. Dolos, T. Kattenborn, and F. E. Fassnacht. How canopy shadow affects invasive plant species classification in high spatial resolution remote sensing. *Remote Sensing in Ecology and Conservation*, 5(4):302–317, 2019.

[39] X. Lu, Z. Liu, F. Zhao, and J. Tang. Comparison of total emitted solar-induced chlorophyll fluorescence (sif) and top-of-canopy (toc) sif in estimating photosynthesis. *Remote Sensing of Environment*, 251:112083, 2020.

[40] S. W. Maier, K. P. Günther, and M. Stellmes. Sun-induced fluorescence: A new tool for precision farming. *Digital imaging and spectral techniques: Applications to precision agriculture and crop physiology*, 66:207–222, 2004.

[41] Z. Malenovskỳ, L. Homolová, R. Zurita-Milla, P. Lukeš, V. Kaplan, J. Hanuš, J.-P. Gastellu-Etchegorry, and M. E. Schaepman. Retrieval of spruce leaf chlorophyll content from airborne image data using continuum removal and radiative transfer. *Remote Sensing of Environment*, 131:85–102, 2013.

[42] Z. Malenovskỳ, O. Regaieg, T. Yin, N. Lauret, J. Guilleux, E. Chavanon, N. Duran, R. Janoutová, A. Delavois, J. Meynier, et al. Discrete anisotropic radiative transfer modelling of solar-induced chlorophyll fluorescence: Structural impacts in geometrically explicit vegetation canopies. *Remote sensing of environment*, 263:112564, 2021.

[43] K. A. Martinez and J. D. Fridley. Acclimation of leaf traits in seasonal light environments: Are non-native species more plastic? *Journal of Ecology*, 106(5):2019–2030, 2018.

[44] K. Maxwell and G. N. Johnson. Chlorophyll fluorescence—a practical guide. *Journal of experimental botany*, 51(345):659–668, 2000.

[45] M. Meroni, M. Rossini, L. Guanter, L. Alonso, U. Rascher, R. Colombo, and J. Moreno. Remote sensing of solar-induced chlorophyll fluorescence: Review of methods and applications. *Remote sensing of environment*, 113(10):2037–2051, 2009.

[46] G. H. Mohammed, R. Colombo, E. M. Middleton, U. Rascher, C. van der Tol, L. Nedbal, Y. Goulas, O. Pérez-Priego, A. Damm, M. Meroni, et al. Remote sensing of solar-induced chlorophyll fluorescence (sif) in vegetation: 50 years of progress. *Remote sensing of environment*, 231:111177, 2019.

[47] M. Mõttus, T. L. Takala, P. Stenberg, Y. Knyazikhin, B. Yang, and T. Nilson. Diffuse sky radiation influences the relationship between canopy pri and shadow fraction. *ISPRS Journal of Photogrammetry and Remote Sensing*, 105:54–60, 2015.

[48] S. Openshaw. The modifiable areal unit problem. *Concepts and techniques in modern geography*, 1984.

[49] J. A. Plascyk. The mk ii fraunhofer line discriminator (fld-ii) for airborne and orbital remote sensing of solar-stimulated luminescence. *Optical Engineering*, 14(4):339–0, 1975.

[50] A. Porcar-Castell, E. Tyystjärvi, J. Atherton, C. Van der Tol, J. Flexas, E. E. Pfündel, J. Moreno, C. Frankenberg, and J. A. Berry. Linking chlorophyll a fluorescence to photosynthesis for remote sensing applications: mechanisms and challenges. *Journal of experimental botany*, 65(15):4065–4095, 2014.

[51] U. Rascher, G. Agati, L. Alonso, G. Cecchi, S. Champagne, R. Colombo, A. Damm, F. Daumard, E. De Miguel, G. Fernandez, et al. Cefles2: the remote sensing component to quantify photosynthetic efficiency from the leaf to the region by measuring sun-induced fluorescence in the oxygen absorption bands. *Biogeosciences*, 6(7):1181–1198, 2009.

[52] O. Regaieg, Y. Wang, Z. Malenovskỳ, T. Yin, A. Kallel, A. Delavois, J. Qi, E. Chavanon, N. Lauret, J. Guilleux, et al. Simulation of solar-induced chlorophyll fluorescence from 3d canopies with the dart model. In *IGARSS 2020-2020 IEEE International Geoscience and Remote Sensing Symposium*, pages 4846–4849. IEEE, 2020.

[53] O. Regaieg, T. Yin, Z. Malenovskỳ, B. D. Cook, D. C. Morton, and J.-P. Gastellu-Etchegorry. Assessing impacts of canopy 3d structure on chlorophyll fluorescence radiance and radiative budget of deciduous forest stands using dart. *Remote Sensing of Environment*, 265:112673, 2021.

[54] M. L. Roderick, G. D. Farquhar, S. L. Berry, and I. R. Noble. On the direct effect of clouds and atmospheric particles on the productivity and structure of vegetation. *Oecologia*, 129:21–30, 2001.

[55] N. Sabater, P. Kolmonen, S. Van Wittenberghe, A. Arola, and J. Moreno. Challenges in the atmospheric characterization for the retrieval of spectrally resolved fluorescence and pri region dynamics from space. *Remote Sensing of Environment*, 254:112226, 2021.

[56] N. Sabater, E. M. Middleton, Z. Malenovsky, L. Alonso, J. Verrelst, K. F. Huemmrich, P. K. Campbell, W. P. Kustas, J. Vicent, S. Van Wittenberghe, et al. Oxygen transmittance correction for solar-induced chlorophyll fluorescence measured on proximal sensing: Application to the nasa-gsfc fusion tower. In *2017 IEEE International Geoscience and Remote Sensing Symposium (IGARSS)*, pages 5826–5829. IEEE, 2017.

[57] N. Sabater, J. Vicent, L. Alonso, J. Verrelst, E. M. Middleton, A. Porcar-Castell, and J. Moreno. Compensation of oxygen transmittance effects for proximal sensing retrieval of canopy–leaving sun–induced chlorophyll fluorescence. *Remote sensing*, 10(10):1551, 2018.

[58] G. Schaepman-Strub, M. E. Schaepman, T. H. Painter, S. Dangel, and J. V. Martonchik. Reflectance quantities in optical remote sensing—definitions and case studies. *Remote sensing of environment*, 103(1):27–42, 2006.

[59] F. D. Schneider, R. Leiterer, F. Morsdorf, J.-P. Gastellu-Etchegorry, N. Lauret, N. Pfeifer, and M. E. Schaepman. Simulating imaging spectrometer data: 3d forest modeling based on lidar and in situ data. *Remote Sensing of Environment*, 152:235–250, 2014.

[60] Y. Sun, L. Gu, J. Wen, C. van Der Tol, A. Porcar-Castell, J. Joiner, C. Y. Chang, T. Magney, L. Wang, L. Hu, et al. From remotely sensed solar-induced chlorophyll fluorescence to ecosystem structure, function, and service: Part i—harnessing theory. *Global Change Biology*, 2023.

[61] T. L. Takala and M. Mõttus. Spatial variation of canopy pri with shadow fraction caused by leaf-level irradiation conditions. *Remote Sensing of Environment*, 182:99–112, 2016.

[62] C. van der Tol, T. Julitta, P. Yang, N. Sabater, I. Reiter, M. Tudoroiu, D. Schuettemeyer, and M. Drusch. Retrieval of chlorophyll fluorescence from a large distance using oxygen absorption bands. *Remote Sensing of Environment*, 284:113304, 2023.

[63] C. van der Tol, N. Vilfan, D. Dauwe, M. P. Cendrero-Mateo, and P. Yang. The scattering and re-absorption of red and near-infrared chlorophyll fluorescence in the models fluspect and scope. *Remote sensing of environment*, 232:111292, 2019.

[64] W. Verhoef and H. Bach. Simulation of hyperspectral and directional radiance images using coupled biophysical and atmospheric radiative transfer models. *Remote sensing of environment*, 87(1):23–41, 2003.

[65] N. Vilfan, C. Van der Tol, P. Yang, R. Wyber, Z. Malenovskỳ, S. A. Robinson, and W. Verhoef. Extending fluspect to simulate xanthophyll driven leaf reflectance dynamics. *Remote sensing of environment*, 211:345–356, 2018.

[66] J. Wang, X. Cao, J. Chen, and X. Jia. Assessment of multiple scattering in the reflectance of semiarid shrublands. *IEEE Transactions on Geoscience and Remote Sensing*, 53(9):4910–4921, 2015.

[67] Y. Wang and J.-P. Gastellu-Etchegorry. Accurate and fast simulation of remote sensing images at top of atmosphere with dart-lux. *Remote Sensing of Environment*, 256:112311, 2021.

[68] Y. Wang, A. Kallel, X. Yang, O. Regaieg, N. Lauret, J. Guilleux, E. Chavanon, and J.-P. Gastellu-Etchegorry. Dart-lux: An unbiased and rapid monte carlo radiative transfer method for simulating remote sensing images. *Remote Sensing of Environment*, 274:112973, 2022.

[69] J.-L. Widlowski, C. Mio, M. Disney, J. Adams, I. Andredakis, C. Atzberger, J. Brennan, L. Busetto, M. Chelle, G. Ceccherini, et al. The fourth phase of the radiative transfer model intercomparison (rami) exercise: Actual canopy scenarios and conformity testing. *Remote Sensing of Environment*, 169:418–437, 2015.

[70] J.-L. Widlowski, M. Taberner, B. Pinty, V. Bruniquel-Pinel, M. Disney, R. Fernandes, J.-P. Gastellu-Etchegorry, N. Gobron, A. Kuusk, T. Lavergne, et al. Third radiation transfer model intercomparison (rami) exercise: Documenting progress in canopy reflectance models. *Journal of Geophysical Research: Atmospheres*, 112(D9), 2007.

[71] H. Wu and Z.-L. Li. Scale issues in remote sensing: A review on analysis, processing and modeling. *Sensors*, 9(3):1768–1793, 2009.

[72] P. Yang, C. van der Tol, P. K. Campbell, and E. M. Middleton. Unraveling the physical and physiological basis for the solar-induced chlorophyll fluorescence and photosynthesis relationship using continuous leaf and canopy measurements of a corn crop. *Biogeosciences*, 18(2):441–465, 2021.

[73] P. Yang, W. Verhoef, and C. van der Tol. The mscope model: A simple adaptation to the scope model to describe reflectance, fluorescence and photosynthesis of vertically heterogeneous canopies. *Remote sensing of environment*, 201:1–11, 2017.

[74] Y. Zeng, G. Badgley, B. Dechant, Y. Ryu, M. Chen, and J. A. Berry. A practical approach for estimating the escape ratio of near-infrared solar-induced chlorophyll fluorescence. *Remote Sensing of Environment*, 232:111209, 2019.

[75] L. Zhang, X. Sun, T. Wu, and H. Zhang. An analysis of shadow effects on spectral vegetation indexes using a ground-based imaging spectrometer. *IEEE Geoscience and Remote Sensing Letters*, 12(11):2188–2192, 2015.

[76] F. Zhao, X. Dai, W. Verhoef, Y. Guo, C. van der Tol, Y. Li, and Y. Huang. Fluorwps: A monte carlo ray-tracing model to compute sun-induced chlorophyll fluorescence of three-dimensional canopy. *Remote sensing of environment*, 187:385–399, 2016.

7 Appendix:

7.1 Appendix 1 - Additive Relationship Between the Algorithm Error and the Illumination Error:

$$F_{\text{retrieved}}(E_{ToC}, L_{ToC}) = F_{ref} \ + \ (1 + \varepsilon_{tot}) \tag{29}$$

$$\varepsilon_{alg} = \ \frac{F(E_{surf}, L_{surf}) - F_{ref}}{F_{ref}} \tag{30}$$

$$\varepsilon_{ill} = \ \frac{F(E_{ToC}, L_{ToC}) - F(E_{surf}, L_{surf})_i}{F(E_{surf}, L_{surf})} \tag{31}$$

$$\varepsilon_{tot} = \ \frac{F(E_{ToC}, L_{ToC}) - F_{ref}}{F_{ref}} \tag{32}$$

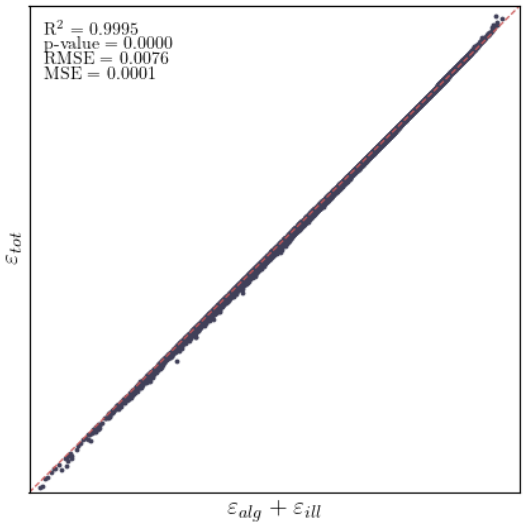

Figure 13: Linear correlation between the total bias ε_{tot} and the sum of both individual biases (ε_{alg}+ε_{ill}). N=1'000'000 Pixels

$$Conclusion: \varepsilon_{tot} \ = \varepsilon_{alg} \ + \varepsilon_{ill} \tag{33}$$

7.2 Appendix 2 - Relationship Between the Shadow Fraction (fSh) and the Illumination Error:

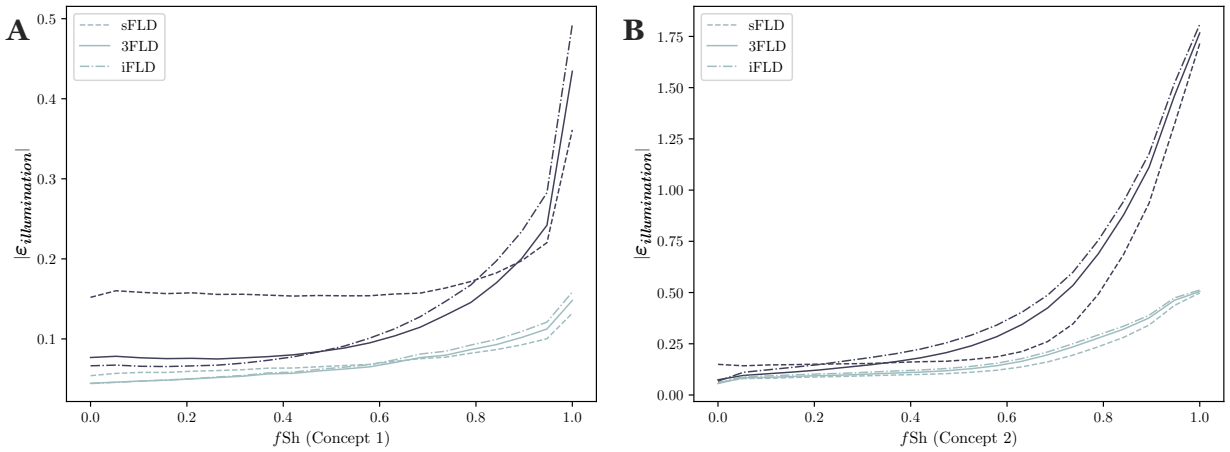

Figure 14: **(A)** Sensitivity of the illumination error to the shadow fraction (fSh) in a classical sense. In this case a pixel is fully shaded when no direct sunlight is present. fSh=1 if E_{dir}=0. **(B)** Sensitivity of the illumination error to fSh from a new perspective. In this case a pixel is fully shaded if there is no influence of direct light at all. fSh=1 if E_{dir} + $E_{GO,dir}$=0. (Dark color: Sun zenith angle SZA=22°, light color: SZA=58°)

7.3 Appendix 3 - Influence of Multiple Scattering within a Broader Wavelength Range:

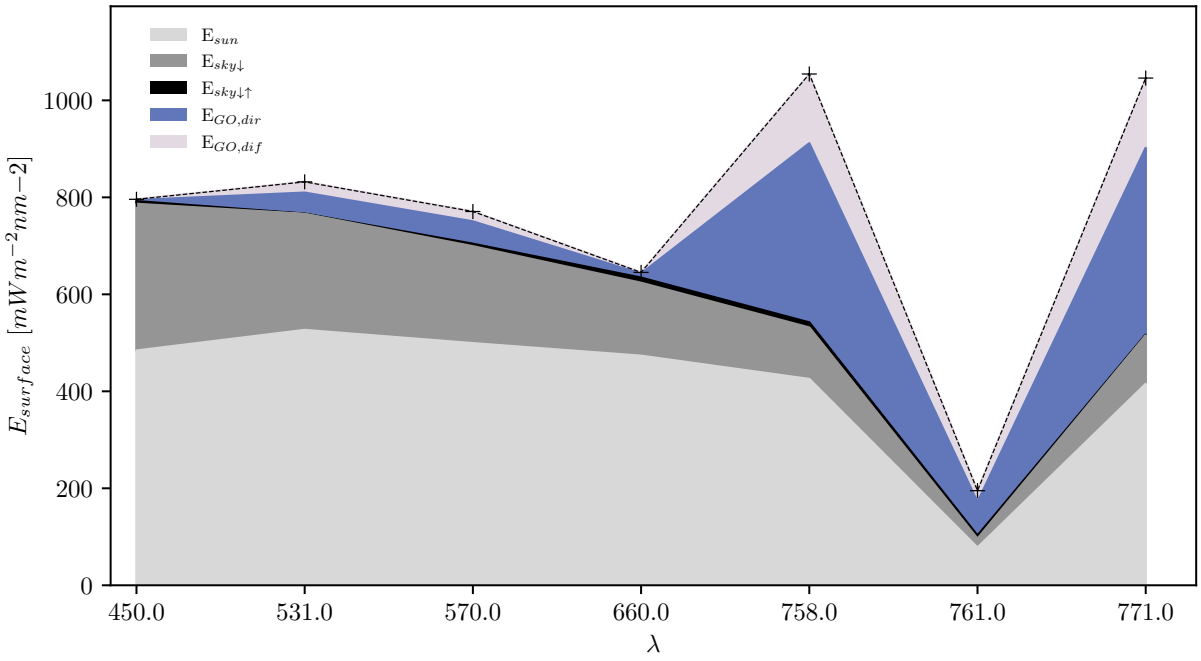

Figure 15: Surface irradiance budget for 7 distinct wavelengths. **VIS:** 450nm, 531nm, 570nm, 660nm. **NIR:** 758nm, 761nm, 771nm. (Grey colors: contributions from sun and sky light, Violet colors: contributions from multiple scattering of initially direct and diffuse light). Plot correspond to illumination conditions at 2PM, SZA=24°

«Personal declaration: I hereby declare that the submitted Thesis is the result of my own, independent work. All external sources are explicitly acknowledged in the Thesis.»